

# Structural performance assessment of full-scale masonry wall systems using operational modal analysis: Laboratory testing and numerical simulations

Andrea Meoni <sup>a,\*</sup>, Antonella D'Alessandro <sup>a</sup>, Michele Mattiacci <sup>a</sup>, Enrique García-Macías <sup>b</sup>, Felice Saviano <sup>c</sup>, Fulvio Parisi <sup>c</sup>, Gian Piero Lignola <sup>c</sup>, Filippo Ubertini <sup>a</sup>

<sup>a</sup> Department of Civil and Environmental Engineering, University of Perugia, Via Goffredo Duranti, 93, Perugia, 06125, Umbria, Italy

<sup>b</sup> Department of Structural Mechanics and Hydraulic Engineering, University of Granada, Campus de Fuentenueva s/n, Granada, 18071, Andalucía, Spain

<sup>c</sup> Department of Structures for Engineering and Architecture, University of Naples "Federico II", Via Claudio, 21, Napoli, 80125, Campania, Italy

## ARTICLE INFO

### Keywords:

Masonry structures  
Structural health monitoring  
Operational modal analysis  
Finite element method  
Structural performance assessment  
Laboratory testing

## ABSTRACT

Operational Modal Analysis (OMA) is a powerful approach to be used in structural performance assessment of historical masonry buildings during their service life. OMA is effective for detecting global damage to masonry buildings, although in some conditions it may exhibit poor sensitivity in detecting local/slight structural damage. Additionally, establishing robust correlations between changes in modal features and the residual load-bearing capacity of monitored buildings is an unresolved task in most of real-world applications. To deepen into these aspects, this paper presents an experimental and numerical program involving two full-scale masonry wall specimens tested under controlled laboratory conditions. Progressive damage was induced in diverse structural settings, and OMA was used to identify the modal features of the wall systems at increasing damage levels. Damage-induced decays in modal features were correlated with performance limit states related to the structures' residual load-bearing capacity, while non-linear Finite Element (FE) models were defined to replicate the tests. The obtained results contribute to filling current research gaps by demonstrating that natural frequencies and mode shapes can be sensitive to local and slight structural damage, also proposing correlations between damage-induced decays in modal features and performance limit states, hence corroborating the use of FE models for replicating damage-induced decays in both vibration frequencies and mode shapes.

## 1. Introduction

Historical masonry buildings, such as towers, churches, and palaces, represent an immeasurably valuable part of Europe's built heritage. Because of their historical importance, these buildings require great efforts by owners and managing authorities for their preservation over time, which commonly result in dense agendas in which maintenance interventions are prioritized according to the current structural condition of every asset. Assessing the structural integrity of existing masonry buildings is often a complex task, because of the peculiar mechanical behavior of these structures that depends largely on their structural design, commonly conceived to resist only static loads, and the inherent heterogeneity of masonry, leading to uncertainties in estimating mechanical properties [1–6]. In addition, the aging of materials, as well as potential structural damages due to natural hazards, such as those from seismic events or ground settlement, can induce modifications in the structural response of existing masonry structures during their service life [7–12].

In the context depicted above, Structural Health Monitoring (SHM) systems can be implemented in existing masonry buildings to aid in the detection of anomalies in their structural performance during their operating conditions. Among the diverse SHM approaches, vibration-based SHM systems exploiting Operation Modal Analysis (OMA) methods have found wide applications to historical masonry buildings over the years, particularly slender structures such as historical residence towers and bells towers [13–19]. These systems are well-suited for masonry buildings because of their non-destructive nature and minimum intrusiveness upon the monitored structure [20]. Their operating principle leverages ambient excitation to perform the dynamic identification of the monitored masonry building, which leads to the estimation of its modal features, such as natural frequencies, mode shapes, and damping ratios, characterizing its dynamic response. Selected modal features are tracked in time by using tailored algorithms so that any changes in their values can be associated with reductions in structural stiffness, i.e., anomalies in structural performance, caused by the development of damage to the monitored building. Prominent

\* Corresponding author.

E-mail address: [andrea.meoni@unipg.it](mailto:andrea.meoni@unipg.it) (A. Meoni).

**Nomenclature**

$\beta$	Relative rotation of the foundation system
$\eta$	Exponent of the Benzeggagh–Kenane fracture energy criterion
$\mu$	Visco-plastic regularization
$\mu_f$	Friction coefficient
$\nu$	Poisson's coefficient
$\psi$	Dilatation angle
$\rho$	Mass density
$\sigma_{b0}$	Initial equibiaxial compressive yield stress
$\sigma_{c0}$	Compressive strength
$\sigma_{c00}$	Initial uniaxial compressive yield stress
$\sigma_{t0}$	Tensile strength
$d_c$	Damage variable in compression
$d_t$	Damage variable in tension
$e$	Flow potential eccentricity
$G$	Tangential elastic modulus
$G_f$	Fracture energy
$G_n$	Fracture energy of the contact interaction in normal direction
$G_s$	Fracture energy of the contact interaction in the first shear direction
$G_t$	Fracture energy of the contact interaction in the second shear direction
$K_c$	Ratio of the second stress invariant on the tensile meridian
$K_{nn}$	Cohesive stiffness in the normal direction
$K_{ss}$	Cohesive stiffness in the first shear direction
$K_{tt}$	Cohesive stiffness in the second shear direction
$K_{xx}^l$	Elastic stiffness of the rotational spring positioned on the top of the left pier along $x$ -axis
$K_{xx}^r$	Elastic stiffness of the rotational spring positioned on the top of the right pier along $x$ -axis
$K_{yy}$	Elastic stiffness of the rotational spring positioned between the wall system and the actuator along $y$ -axis
$K_{yy}^l$	Elastic stiffness of the rotational spring positioned on the top of the left pier along $y$ -axis
$K_{yy}^r$	Elastic stiffness of the rotational spring positioned on the top of the right pier along $y$ -axis
$K_z$	Elastic stiffness of the spring positioned between the wall system and the actuator along $z$ -axis
$K_z^r$	Elastic stiffness of the spring positioned on the top of the right pier along $z$ -axis
$t_n$	Maximum allowable traction stress in normal direction
$t_s$	Maximum allowable traction stress in the first shear direction
$t_t$	Maximum allowable traction stress in the second shear direction
$u_{t0}$	Cracking displacement at which complete loss of strength takes place
$u_t$	Cracking displacement

applications of vibration-based SHM systems exploiting OMA methods to historical masonry buildings can be found in [21–29]. In this context, the removal of environmental effects from the tracked modal features is a task of the utmost importance [30,31]. Although the effectiveness of OMA approaches for detecting global damage to masonry buildings by assessing changes in their modal features is widely recognized

by the scientific community [32–34], OMA methods are sometimes criticized for their lack of sensitivity to local and/or slight defects. As an additional drawback, establishing clear correlations between changes in modal features and the residual load-bearing capacity of monitored buildings is often a difficult task in most real-world applications. In the last years, laboratory tests have been conducted to study the effectiveness of OMA methods applied to masonry structures under controlled environmental and loading conditions. Investigations have been carried out to study the sensitivity of modal features to earthquake-induced damage in full-scale masonry buildings subjected to shaking table tests [35–37] and other damage scenarios, also involving various masonry structural elements, such as vaults, arches, and panels [38–42]. Efforts have also been made to study the contribution of masonry infill walls on the dynamic response of infilled buildings through OMA methods, by exploring diverse geometry configurations, damage scenarios, and more [43,44].

The aforementioned works demonstrate certain correlations between structural damage and decays of modal features (especially vibration frequencies), and some of them validate the results obtained via experimental testing by using numerical models aimed at reproducing the decays observed in the proposed modal-based damage indicators. Nonetheless, a comprehensive study that (i) demonstrates the clear sensitivity of both natural frequencies and mode shapes to local/slight structural damage, (ii) validates this result by proposing correlations between decays in modal features and widely accepted performance limit state formulations, and (iii) corroborates the ability of numerical models to reproduce, after proper calibration, both decays in vibration frequencies and mode shapes, thus promoting their use for interpreting the results from experimental testing, appears to be lacking in the state of the art. In detail, establishing sound correlations between damage-induced decays in modal features and performance limit states is a key to enable the vibration-based structural integrity assessment of the monitored structure, also facilitating the extension of the results from laboratory testing to real-field SHM applications. Furthermore, the identification of numerical models capable of reproducing both decays in vibration frequencies and mode shapes can contribute to justify their use in model-based SHM applications to masonry structures. This paper aims to contribute to filling these gaps in the state of the art by presenting an experimental and numerical program involving two full-scale masonry wall systems constructed and subjected to controlled laboratory testing under progressive damage conditions by reproducing diverse structural settings. The modal features of the wall systems were estimated by exploiting ambient excitation at each step of the test sequence, and the damage-induced variations in the modal features were compared to the developed damage pattern and proposed limit state formulations. Non-linear FE models were developed to numerically reproduce the tests conducted on the wall systems and were used to interpret the experimental findings.

The organization of the paper is as follows. Section 2 outlines the experimental methodology adopted to construct and test the wall systems, along with the adopted approach to assess their structural integrity. Section 3 describes the developed numerical models and details the numerical analyses performed to reproduce the experimental tests. Section 4 presents the outcomes from the experimental and numerical investigations and, finally, Section 5 closes the paper with some concluding remarks.

## 2. Experimental methodology

This section details the diverse aspects included in the experimental program. Firstly, the case study structures and the test setups are described. Afterwards, the methodologies adopted to induce progressive damage to the specimens, to perform their modal identification, and to carry out damage detection and vibration-based structural performance assessment are presented.

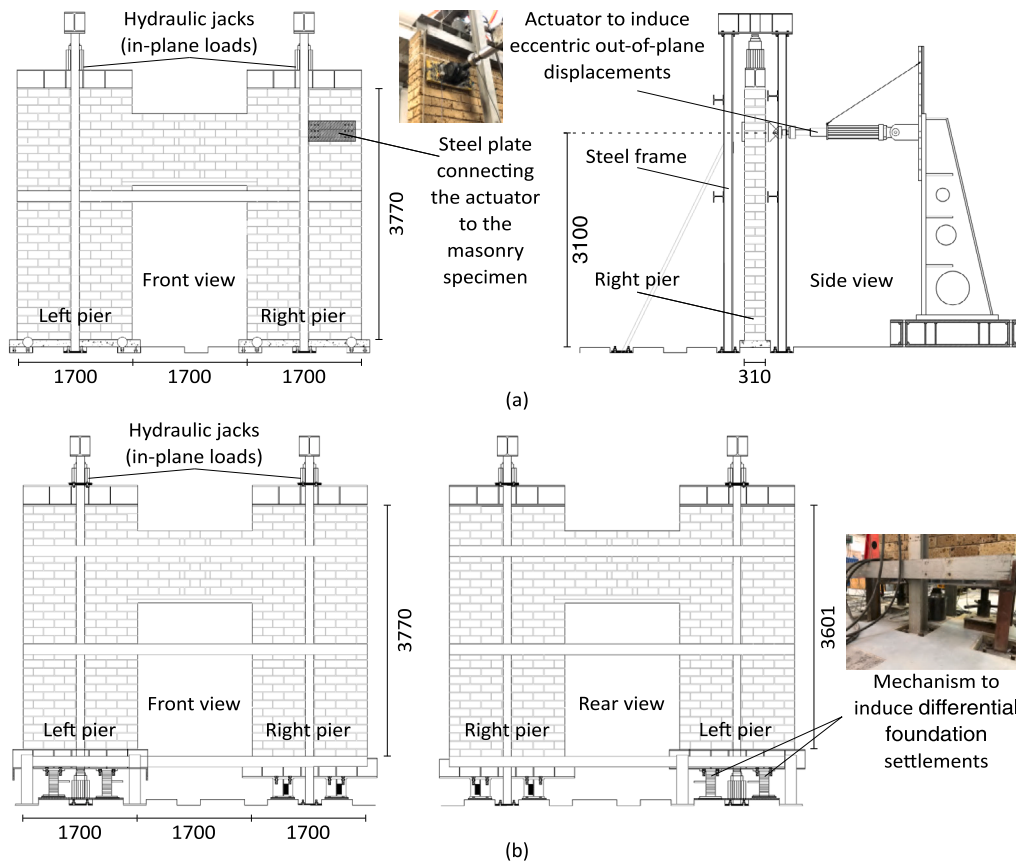


Fig. 1. Case study specimens: (a) masonry wall system tested under eccentric out-of-plane loading conditions (Specimen A); (b) masonry wall system tested under differential foundation settlements (Specimen B) (units in mm).

## 2.1. Description of masonry specimens

The case study structures, consisting of two full-scale masonry wall systems, each with a central opening and two piers connected to each other by a spandrel panel and a wooden lintel, were constructed and tested at the Testing Laboratory of the Department of Structures for Engineering and Architecture of the University of Naples Federico II. The specimens were designed in agreement with benchmark wall systems tested by Parisi et al. [45,46] in previous studies on the in-plane seismic capacity of unreinforced masonry walls with openings. This allows future comparative studies on both in-plane and out-of-plane capacity of those wall systems. Both specimens were constructed by arranging  $300 \times 150 \times 110 \text{ mm}^3$  tuff stones, with mortar layers having thickness of 10 mm, arranged in a double-leaf running-bond pattern. The thickness of the mortar layers was reduced in plan to about  $3/4$  of the full thickness to simulate the mechanical response of aged masonry walls (i.e., the material degradation due to mortar aging). Fig. 1(a) depicts the main geometrical dimensions of the wall system tested under out-of-plane loading conditions, hereafter referred to as Specimen A. In this case, a hydraulic actuator, which was connected to the pier on the right-hand side of the structure by means of two bolted steel plates, was used to impose eccentric out-of-plane displacements to the wall system, as later specified in Section 2.2. Because the tests presented in this work are part of a broader experimental program framed within the DETECT-AGING research project (see Acknowledgments), the reader is to be aware that this loading condition was considered primarily to investigate the role of the spandrel in the structural response of masonry structures when subjected to non-uniform out-of-plane loads which may originate from the degradation of tie rods or unbalanced thrust of vaults. Hydraulic jacks, positioned on top of a steel frame to prevent potential ruinous overturning of the wall system, were used to

simulate the effects of dead loads acting on the structure. Rigid steel beams were placed between the jacks and the top of the masonry piers to ensure a uniform distribution of compressive stresses. The second specimen, henceforth referred to as Specimen B, was tested under differential settlements with the structural setting shown in Fig. 1(b). The structure was built on steel foundations that hosted, on the left side, a hand-operated steel mechanism to induce settlements to the foundation of the pier. Because of the presence of this hand-operated steel mechanism, the left pier of Specimen B was slightly shorter than the right one, differently to Specimen A, the piers of which had the same length. Hydraulic jacks mounted on a steel frame were also used in this structural setting to apply dead loads on both piers.

Both the masonry specimens were instrumented with a dense network of single-axis seismic accelerometers, model PCB393B12, with a sensitivity of 10 V/g. The sensors, mounted on supporting L-shaped steel plates screwed to the tuff stones, were used to record the microvibrations of the structural systems under ambient excitation. A detailed representation of the positioning and measurement direction of each accelerometer mounted on the specimens is shown in Fig. 2. The sensor configurations in both specimens are quite similar, although two additional accelerometers (channels 6 and 8) were added to Specimen B with respect to Specimen A. The purpose of this denser configuration is to provide a more refined discretization of the end areas of the spandrel panel, where cracks were expected to develop as a result of the foundation settlements.

## 2.2. Testing procedures

Specimen A was initially loaded in its plane by applying a vertical force of 400 kN on each of its piers to simulate dead loads. Subsequently, the wall specimen was subjected to eccentric out-of-plane

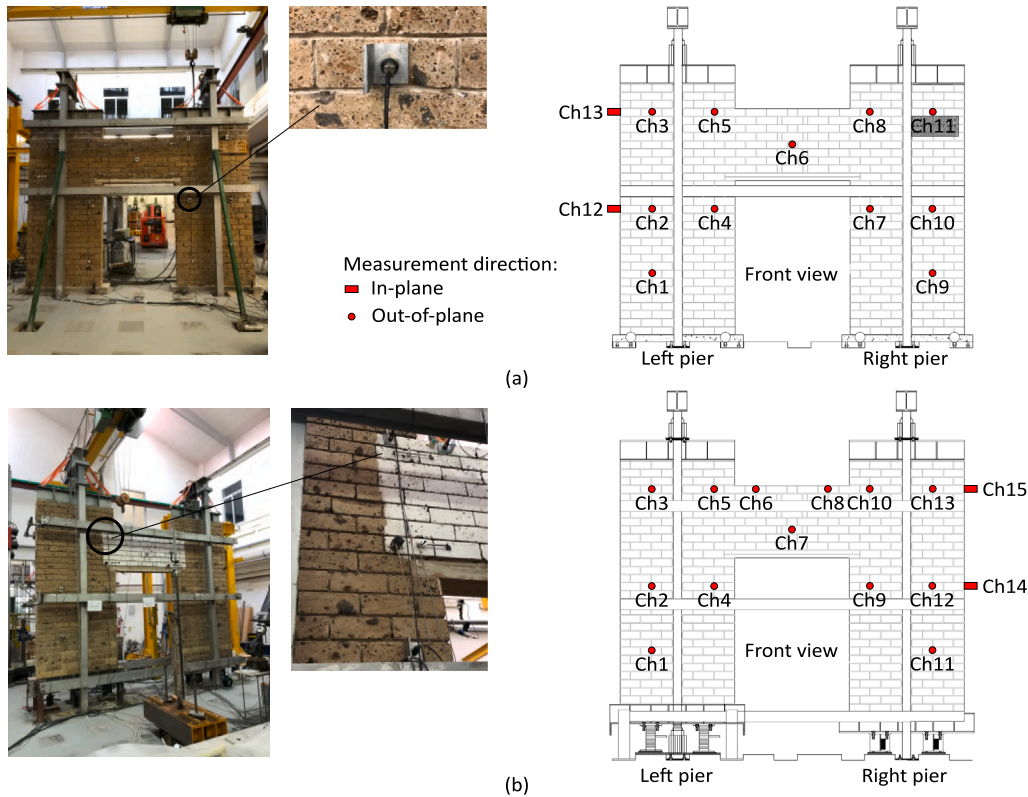


Fig. 2. Front view, detail, and schematic positioning of the accelerometers on the case study structures: (a) masonry wall system tested under eccentric out-of-plane loading conditions (Specimen A); (b) masonry wall system tested under differential foundation settlements (Specimen B).

displacements of increasing magnitude according to the test sequence reported in Table 1, which also specifies the out-of-plane drift ratio, corresponding to the percentage ratio of the out-of-plane displacement to the height of the horizontal actuator, imposed to the wall system at every step of the test. Initially, a settling cycle (D1) was performed on the structure by imposing an out-of-plane displacement of 3.00 mm, then returning to the initial configuration and pushing the wall system of 3.00 mm out of plane again. Following this, monotonically increasing out-of-plane displacements, from 9.00 mm to 93.36 mm (corresponding to an out-of-plane drift ratio equal to 3.01%, this last defined as the percentage ratio between the out-of-plane displacement and the height of the horizontal actuator), were imposed on the structure by performing steps D2 to D7.

Specimen B was loaded in its plane by applying a vertical force of 200 kN on each of its piers, followed by progressive damage conditions induced by increasing differential settlements at the foundation of the left pier according to the test sequence reported in Table 2. Even in this case the table outlines the value of the in-plane drift ratio, corresponding to the percentage ratio of the foundation settlement to the distance between the piers' center lines, applied to the wall system at each step of the test. A settlement of 3.00 mm was imposed at step S2, followed by incremental settlements of 6.00 mm until S4 (from 3.00 mm to 15.00 mm). Finally, in step S5, the structure was subjected to a settlement of 35.00 mm (corresponding to an in-plane drift ratio equal to 1.03%, this last defined as the percentage ratio between the foundation settlement and the distance between the piers' center lines). Visual inspections were carried out on both specimens before and after each step of the test sequences to identify the developed crack pattern. It is worth noting that the above definition of drift ratios is an attempt to facilitate the generalization of the test methodologies and results presented in this work to structures with different geometric characteristics. In this regard, the reader is to be aware that the magnitude of the drift ratios (with reference to both the case of out-of-plane displacements and foundation settlements) imposed to the wall systems

was designed to induce the formation of severe crack patterns in the tested masonry specimens while preventing their ruinous collapse for safety reasons.

After every step in the loading sequence, Ambient Vibration Tests (AVTs) were performed to characterize the modal signatures of the wall systems. A data acquisition system model NI cDAQ-9188, equipped with three vibration input modules model NI-9234, was used to manage the acquisition of the acceleration signals from the sensors mounted on the specimens. The sampling frequency was set to 1653 Hz, which corresponds to the minimum sampling rate operable by the adopted vibration input modules in accordance with their hardware anti-aliasing filters, and each measurement record was 15 min long. This time window is much longer than 2000 times the fundamental period of the specimens, which is typically recommended in the literature to ensure accurate estimation of the modal parameters [47].

### 2.3. Modal identification and damage detection

The OMA software MOVA [48] was used to carry out the modal identification of the masonry wall systems. Firstly, the acquired acceleration signals were detrended and resampled at 100 Hz. Then, the Enhanced Frequency Domain Decomposition (EFDD) method was employed to estimate the modal features of the case study structures, namely their natural frequencies, damping ratios, and mode shapes. Specifically, the resonant peaks were first selected through peak-picking analysis of the first singular value of the spectral matrix of accelerations. Then, the mode shapes were identified through the first singular vectors at the selected frequencies, and the natural frequencies and damping ratios were estimated through the natural excitation technique (NExT) and the Ibrahim time-domain method (bell extraction considering a Modal Assurance Criterion (MAC) threshold of 0.8). The Modal Phase Co-linearity (MPC) index was used to evaluate the modal complexity of the mode shapes associated with the identified natural frequencies, thus aiding in corroborating the identification of structural

**Table 1**

Sequence of incremental eccentric out-of-plane displacements applied to Specimen A (note that the out-of-plane drift ratio corresponds to the percentage ratio of the out-of-plane displacement to the height of the horizontal actuator).

Step No.	Typology	Out-of-plane displacement [mm]	Out-of-plane drift ratio [%]
D1	Settling cycle (reference condition)	3.00	0.10
D2	Progressive damage	9.00	0.29
D3	Progressive damage	18.00	0.58
D4	Progressive damage	27.00	0.87
D5	Progressive damage	36.00	1.16
D6	Progressive damage (peak force)	58.00	1.87
D7	Progressive damage	93.36	3.01

**Table 2**

Sequence of incremental foundation settlements applied to Specimen B (note that the in-plane drift ratio corresponds to the percentage ratio of the foundation settlement to the distance between the piers' center lines).

Step No.	Typology	Foundation settlement [mm]	In-plane drift ratio [%]
S1	Reference condition	0.00	0.00
S2	Progressive damage	3.00	0.09
S3	Progressive damage	9.00	0.26
S4	Progressive damage	15.00	0.44
S5	Progressive damage	35.00	1.03

vibration modes, since structural modes are typically characterized by low modal complexity, i.e., their mode shapes can be well described using real numbers (in this work, this last circumstance corresponds to a MPC index equal to 100%) [34,49–51].

The effects of the progressive damage were assessed by evaluating the modifications in the modal features of the specimens with respect to their reference (healthy) configurations. Specifically, the decays in the natural frequencies were evaluated in terms of relative variations, while the consistency between the identified mode shapes was assessed by using the MAC [52]. On Specimen A, the reference modal baseline was determined after the execution of step D1 when the wall system was still in sound condition. In the case of Specimen B, the reference modal baseline was determined after the execution of step S1. It is important to remark that the AVTs were conducted on both wall systems under stable temperature and humidity conditions and, thus, the influence of environmental effects on the estimated modal properties was negligible.

#### 2.4. Structural integrity assessment

The evaluation of the structural integrity of the wall systems was carried out by establishing a correlation between the decay of modal features and their residual load-bearing capacity at progressive damage states. To this end, widely accepted limit state formulations for the investigated structural settings were considered [53], including quantitative/qualitative force/ displacement thresholds related to Serviceability Limit States (SLSs) and Ultimate Limit States (ULSs). On this basis, the variations in the modal properties induced by damage (decays in natural frequencies and MAC indexes) were computed at every threshold by linearly interpolating the decay trends obtained from the data processing performed in Section 2.3.

For Specimen A, the limit state formulations provided by the Italian Building Code [54] for seismic assessment were adopted, since the application of increasing out-of-plane displacements experimentally simulated a pushover analysis [55]. On this basis, the SLSs accounted for the Operational Limit State (OLS—no significant structural damage) and the Damage Limitation Limit State (DLLS—no significant reduction of the load-bearing capacity). On the other hand, the Life Safety Limit State (LSLS—significant loss of stiffness against horizontal actions) and the Collapse Limit State (CLS—small margin of safety against collapse due to horizontal actions) were considered as ULSs. Similarly, for Specimen B, the limit state formulations provided by Eurocode [56] for geotechnical design were considered to evaluate reductions in the load-bearing capacity of the wall system under increasing settlement

of the left pier foundation. The relative rotation of the foundation system,  $\beta$ , was computed for each step of the test sequence, hence compared with the relative rotation associated with the reaching of the SLS,  $\beta_{SLS} = 1/500$ , and that indicating the attainment of the ULS,  $\beta_{ULS} = 1/150$ .

### 3. Numerical simulations

Two non-linear 3D mechanical models, discretized numerically with the FE method in Abaqus [57], were defined to simulate the experimental tests carried out on the masonry specimens. The outcomes from the numerical analyses were used to aid the interpretation of the decays observed in the modal features of the masonry wall systems caused by the imposed progressive structural damage, thus demonstrating the ability of FE models to replicate damage-induced changes in both vibration frequencies and mode shapes and, to some extent, supporting the use of model-based damage identification approaches combined with OMA methods for SHM of masonry structures. In the following, the common features of the numerical simulation of the two masonry walls are presented. Subsequently, the features that distinguish numerical models from each other, such as mechanical properties, contact interactions, and boundary conditions, are described in detail.

#### 3.1. Mechanical response of masonry

Due to the large size of the tested specimens, a macro-modeling approach was considered to reproduce the mechanical behavior of the masonry as a homogenized continuous element [58–61]. The Concrete Damage Plasticity (CDP) model for quasi-brittle materials [62–65] was adopted to simulate the non-linear mechanical response of the masonry. The CDP model is able to reproduce damage in tension and compression through two dimensionless damage parameters, namely  $d_t$  and  $d_c$ , respectively. These parameters induce an isotropic degradation of the elastic modulus, in such a way that  $d_{c,t} = 0$  and  $d_{c,t} = 1$  represent the limit conditions of undamaged and total loss of stiffness, respectively. In this work, the post-failure behavior of the masonry in tension following the Hillerborg's fracture energy criterion [66] was adopted. Furthermore, the elastic stiffness degradation was defined in terms of cracking relative displacements (crack widths) instead of cracking strains. This was done to limit the effect of the mesh size on the outcomes from numerical analyses (i.e., mesh sensitivity of the FE models). The degradation of elastic stiffness in compression was neglected given that the experiments revealed that the developed

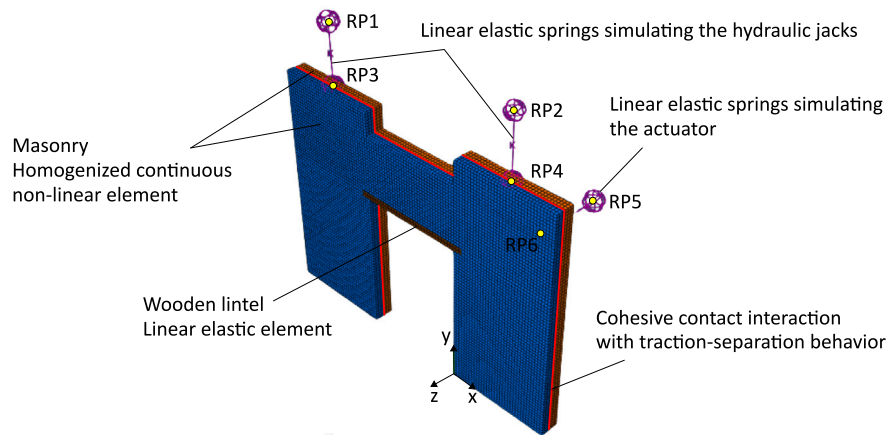


Fig. 3. Three-dimensional FE model for the simulation of the masonry wall system subjected to increasing out-of-plane displacements (Specimen A).

damage patterns were primarily driven by excessive tensile stresses. The plastic damage parameters used to specialize the non-linear mechanical response of masonry in the performed numerical simulations, including flow potential eccentricity,  $e = 10$ , dilatation angle,  $\psi = 0.1^\circ$ , ratio between the initial equibiaxial compressive yield stress and initial uniaxial compressive yield stress,  $\sigma_{b0}/\sigma_{c00} = 1.16$ , ratio of the second stress invariant on the tensile meridian,  $K_c = 0.667$ , and viscoplastic regularization term,  $\mu = 1.0E - 4$ , were assumed from literature Refs. [67–69].

### 3.2. Simulation of the out-of-plane loading conditions - Specimen A

In Specimen A, the observed damage pattern reported hereafter in Section 4.2 revealed the onset of a vertical crack crossing the thickness of the wall. To reproduce this damage mechanism, it was critical to explicitly allow the formation of the observed crack through cohesive elements. On this basis, the numerical model was defined by means of two homogenized continuous non-linear masonry elements coupled by a cohesive general contact interaction crossing the thickness of the wall, as shown in Fig. 3. The wooden lintel, modeled with a linear elastic behavior, was connected to the other parts of the model through a tie constraint. A mesh composed of 49,393 nodes and 35,448 C3D8R linear hexahedral elements with size of 50 mm was adopted to discretize the geometry of the model. The mechanical response of the contact interaction was specialized with a traction–separation behavior. In particular, damage at the contact level was assumed to initiate when a quadratic interaction function involving the contact stress ratios reached a value of one (quadratic traction criterion). The damage evolution law, which describes the rate of degradation of the cohesive stiffness, was defined using the Benzeggagh–Kenane fracture energy criterion, in which linear softening was considered [70,71]. Compressive and friction behaviors were also implemented in the cohesive contact. The hard contact criterion was set in the normal direction to adjust the contact response only when the slave nodes are in touch with the master surfaces. Cohesive behavior contributes to normal contact stress only when the slave nodes attempt to detach themselves from the master surfaces. The penalty friction method was assumed in the tangential direction. In this case, the selected friction law is only activated when the cohesive contact is degraded. To take into account the constraints imposed by the hydraulic jacks during the ambient vibration tests, linear elastic springs were implemented in the model to stiffen the displacements of the piers along the  $z$ -axis and the rotations around the  $y$ -axis (Fig. 3). On their upper side, springs were connected to a Reference Point (RP) constrained in all degrees of freedom (RP1 and RP2 for the left and right pier, respectively). On their lower side, springs were linked to an additional RP anchored in turn to the top surface of each pier via a kinematic constraint (RP3

and RP4 for the left and right pier, respectively). Linear elastic springs were also implemented into the model to stiffen the displacements of the right pier along the  $z$ -axis and rotations around the  $y$ -axis, thus simulating the connection between the wall system and the actuator. From the side of the actuator, springs were connected to RP5, which was constrained in all degrees of freedom. In the opposite direction, springs terminated on RP6, which was in turn connected to a portion of the abutment via a kinematic constraint. The actuator-pier connection area resembled in geometry the steel plate adopted in the experimental structural setting. Finally, the piers were fixed to the ground during the numerical analyses.

Dead loads were simulated by applying an axial pressure of 0.76 MPa on the top surface of each pier, while out-of-plane loading conditions were simulated by imposing incremental displacements to RP5 along the  $z$ -axis according to the test sequence reported in Table 1. Non-linear modal analyses based on linear perturbation were carried out by considering the tangent stiffness matrix before and after each step of the test sequence to determine the resonant frequencies and corresponding mode shapes of the numerical model. These were adopted to interpret the decay of the modal features observed experimentally by testing the wall specimen under eccentric out-of-plane loading conditions. The mechanical properties set in the numerical analyses to specialize the response of the model are collected in Table 3. The mechanical parameters of the wooden lintel come from [72]. The elastic modulus of the masonry was taken from [73], while its Poisson's coefficient was computed as suggested by the Eurocode 6 from linear Elasticity Theory [74], namely according to the relation  $G = E/2(1+\nu)$ , with  $G$  being the tangential elastic modulus from [73]. Prior to the simulation of the out-of-plane loading conditions, the mass density of the masonry,  $\rho$ , the stiffness of the springs, and that of the cohesive contact interaction were fine-tuned to match the reference modal features characterizing the first two modes of vibration of the wall system obtained experimentally from the modal identification carried out after the execution of step D1 of the test sequence (see Section 4.1). Specifically, the mass density was decreased by about 2.32% compared to its initial value from [73], while values of the elastic stiffness of the springs, being closely related to the boundary conditions of the tested wall system, were manually adjusted to numerically replicate the dynamic behavior of the specimen without considering specific references from the literature nor from experimental testing. Similarly, stiffness values of the cohesive contact interaction were determined to make the dynamic response of the FE model with contact interaction equal to that of the same FE model yet without contact layer. Afterwards, the tensile strength of the masonry,  $\sigma_{t0}$ , its fracture energy,  $G_f$ , the tensile damage parameter,  $d_n$ , the cracking displacement,  $u_t$ , and the maximum allowable traction stress in the first and second shear direction,  $\tau_s$  and  $\tau_t$ , respectively, were adjusted to mimic the cracking pattern obtained experimentally on Specimen A

**Table 3**  
Mechanical properties used to specialize the response of the numerical model of Specimen A.

Wooden lintel			
$E = 8000 \text{ MPa}$	$\nu = 0.25$	$\rho = 650 \text{ kg/m}^3$	
Masonry			
$E = 1200 \text{ MPa}$	$\nu = 0.20$	$\rho = 1720 \text{ kg/m}^3$	$G_f = 0.012 \text{ N/mm}$
$\sigma_{c0} = 2.05 \text{ MPa}$	$\sigma_{t0} = 0.1 \text{ MPa}$		
$d_c$	$\bar{\epsilon}_c^{in}$	$d_t$	$u_t$
0.00	0.0000	0.00	0.0000
		0.15	0.0825
		0.90	0.1100
Cohesive contact interaction			
Cohesive behavior			
$K_{nn} = 4000 \text{ N/mm}^3$	$K_{ss} = 4000 \text{ N/mm}^3$	$K_{tt} = 4000 \text{ N/mm}^3$	
Damage initiation			
$t_n = 0.25 \text{ MPa}$	$t_s = 0.18 \text{ MPa}$	$t_t = 0.18 \text{ MPa}$	
Damage evolution			
$\eta = 2$	$G_n = 0.018 \text{ N/mm}$	$G_s = 0.125 \text{ N/mm}$	$G_t = 0.125 \text{ N/mm}$
Tangential behavior			
$\mu = 0.6$			
Springs on top of the piers			
$K_z^r = 1200 \text{ N/mm}$	$K_{yy}^r = 4.1\text{E}+9 \text{ Nmm/radian}$	$K_{yy}^l = 4.24\text{E}+9 \text{ Nmm/radian}$	
Springs connecting the wall system with the actuator			
$K_z = 24000 \text{ N/mm}$	$K_{yy} = 4.24\text{E}+9 \text{ Nmm/radian}$		

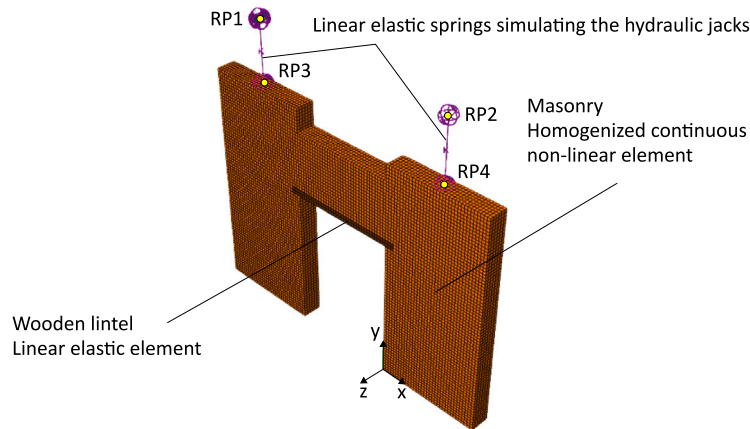


**Fig. 4.** Three-dimensional FE model for the simulation of the masonry wall system subjected to increasing differential foundation settlements (Specimen B).

at each stage of the test sequence (see Section 4.2). In this case,  $\sigma_{t0}$  was determined by considering the empirical relation  $0.1\sigma_{c0}$ , with  $\sigma_{c0}$  from [73], then decreasing this value by 50%. The fracture energy,  $G_f$ , was established by reducing by about 34% the value obtained from the dynamic characterization of the mechanical properties of tuff masonry reported in [75], also in view of the closer resemblance of the tuff masonry tested in this work with that used in [76]. The value of  $u_{t0}$  was determined through the relation  $u_{t0} = 2G_f/\sigma_{t0}$  from [57], while values set for  $d_t$  and  $u_t$  were manually calibrated to numerically replicate crack initiation and propagation observed from experimental testing. The values set for  $t_s$  and  $t_t$  were initially taken from [70], and then manually reduced by 28% to match the experimental cracking pattern. The remaining mechanical parameters adopted to specialize the response of the cohesive contact interaction come from [70]. Despite the performed manual calibration, it should be noted that the ratio of elastic modulus to compressive strength is about 600, denoting realistic modeling of the mechanical behavior of masonry [77–79]. The Abaqus implicit solver was adopted to run the numerical analyses.

### 3.3. Simulation of the differential foundation settlements - Specimen B

The numerical model replicating Specimen B consisted of a unique homogenized continuous non-linear masonry element tied to a linear

elastic part representing the wooden lintel, as shown in Fig. 4. A mesh composed of 41,944 nodes and 34,272 C3D8R linear hexahedral elements with 50 mm size was adopted to discretize the geometry of the model. Dead loads were simulated by applying an axial pressure of 0.38 MPa on the top surface of each pier. Similarly to the previous model, linear elastic springs were implemented in the model to reproduce the connection with the hydraulic jacks. In this case, elastic springs were used to stiffen the rotations of both piers around the  $x$ -axis. The simulation of the stiffening effect involved connecting each spring to a reference point, which in turn was attached to the top of each pier by means of a kinematic constraint. Specifically, for the left and right piers, the springs were connected to RP3 and RP4, respectively. At the top, each spring was connected to an additional reference point (RP1 and RP2 for the left and right piers, respectively). These points were fixed in all degrees of freedom. Initially, the basement of the piers was constrained to the ground to simulate the experimental structural setting of step S1 of the test sequence. Then, to mimic the occurrence of differential settlements at the left foundation of the wall specimen, incremental vertical displacements were imposed to the basement of the corresponding pier of the numerical model, by following the test sequence outlined in Table 2. Non-linear modal analyses, based on linear perturbation considering the tangent stiffness matrix, were carried out both before and after each step of the test sequence to determine the

**Table 4**  
Mechanical properties used to specialize the response of the numerical model of Specimen B.

Wooden lintel			
$E = 8000 \text{ MPa}$	$\nu = 0.25$	$\rho = 650 \text{ kg/m}^3$	
Masonry			
$E = 720 \text{ MPa}$	$\nu = 0.2$	$\rho = 1720 \text{ kg/m}^3$	$G_f = 0.014 \text{ N/mm}$
$\sigma_{c0} = 2.05 \text{ MPa}$	$\sigma_{c0} = 0.28 \text{ MPa}$		
$d_c$	$\epsilon_c^{in}$	$d_t$	$u_t$
0.00	0.0000	0.00	0.0000
		0.97	0.1120
Springs at the top of the piers			
$K_{xx}^r = 4.6E+8 \text{ Nmm/radian}$	$K_{xx}^l = 4.6E+8 \text{ Nmm/radian}$		

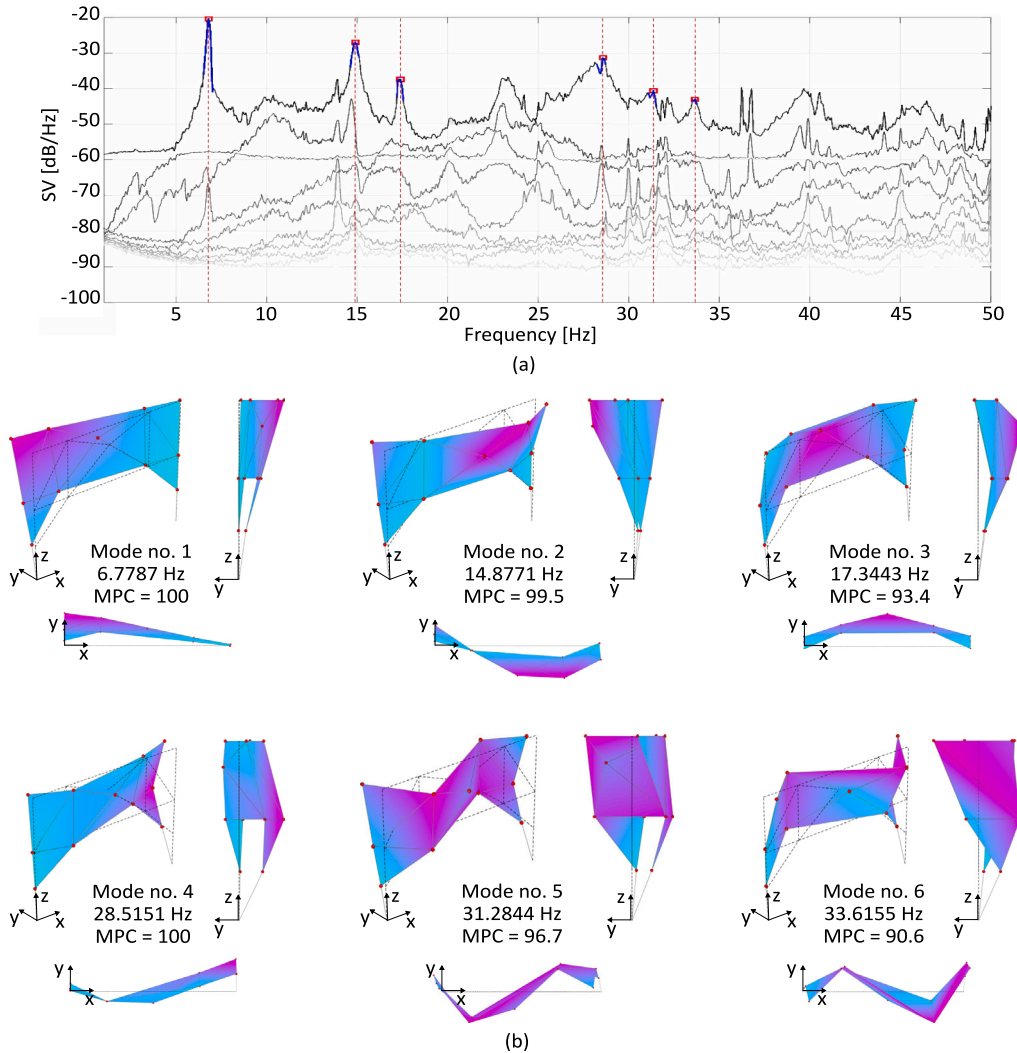


Fig. 5. Experimental modal identification of Specimen A after step D1: (a) singular values of the spectral density matrix; (b) reference modal features.

resonant frequencies and corresponding mode shapes characterizing the dynamic response of the numerical model. Hence, the obtained numerical outcomes were used to interpret the decay of the modal features of the wall system observed experimentally. Table 4 collects the mechanical properties set in the numerical analyses to characterize the response of the numerical model. A manual calibration of the elastic modulus of the masonry,  $E$ , its mass density,  $\rho$ , and the stiffness of the springs was carried out to match the features of the first two modes of vibration of the wall system that were obtained from the

modal identification performed after the execution of step S1 of the test sequence (see Section 4.1). In particular, the mass density and the Poisson's coefficient characterizing the FE model of Specimen A were also adopted to specialize the numerical model of Specimen B, yet the elastic modulus set in the latter was obtained by reducing by 40% the value set in the FE model of Specimen A. As before, values of the elastic stiffness of the springs, being closely related to the boundary conditions of the tested wall system, were manually adjusted to numerically replicate the reference dynamic behavior of the tested

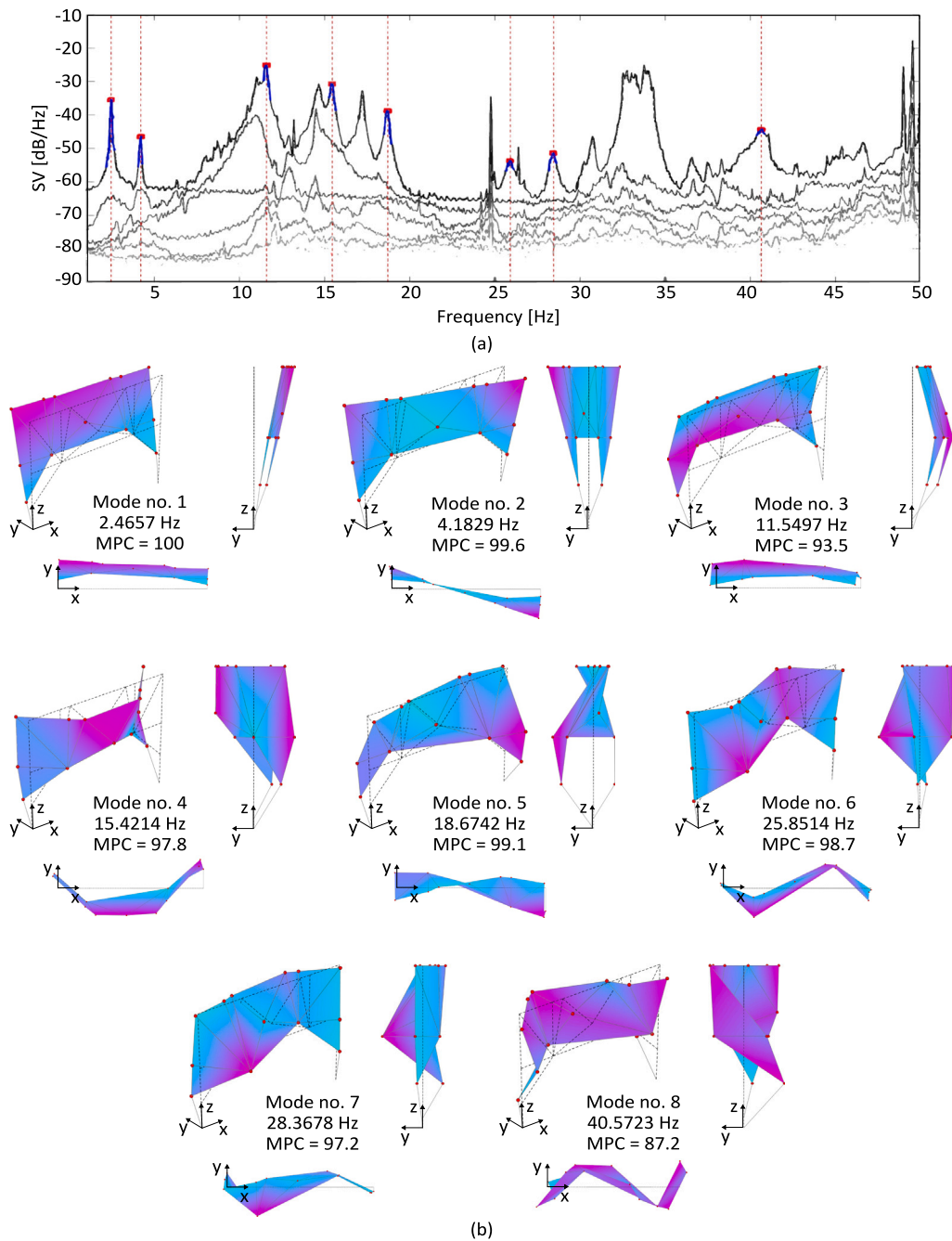


Fig. 6. Experimental modal identification of Specimen B after step S1: (a) singular values of the spectral density matrix; (b) reference modal features.

specimen. Subsequently, the tensile strength of the masonry,  $\sigma_{t0}$ , its fracture energy,  $G_f$ , the tensile damage parameter,  $d_t$ , and the cracking displacement,  $u_t$ , were fine-tuned to replicate, at each stage of the test sequence, the cracking pattern that developed experimentally on Specimen B (see Section 4.2). Specifically,  $\sigma_{t0}$  was determined as in the case of Specimen A, yet by increasing the value from the relation  $0.1\sigma_{c0}$  by about 37%. The fracture energy,  $G_f$ , was defined by reducing by about 23% the value obtained from [75]. Lastly, the parameters  $d_t$  and  $u_t$  were defined like in the case of Specimen A. It is worth pointing out that Specimens A and B were built with the same construction materials (i.e., tuff stones from the same quarry and mortar of similar mix design), but at different times. Variability in the laying of the masonry also cannot be completely excluded between the specimens. The curing conditions of the wall systems may also have been slightly different at the time of testing. These aspects justify the discrepancies

that can be noted between the mechanical properties that specialize the numerical models of Specimens A and B, with particular reference to the elastic modulus of the masonry and its tensile strength.

#### 4. Results and discussion

This section presents the results obtained in the experimental program and the outcomes from numerical simulations. Specifically, the identification of the reference modal properties of the walls is reported in Section 4.1.

##### 4.1. Reference modal features

Figs. 5 and 6 illustrate the results obtained from the modal identification of Specimens A and B carried out after the execution of steps

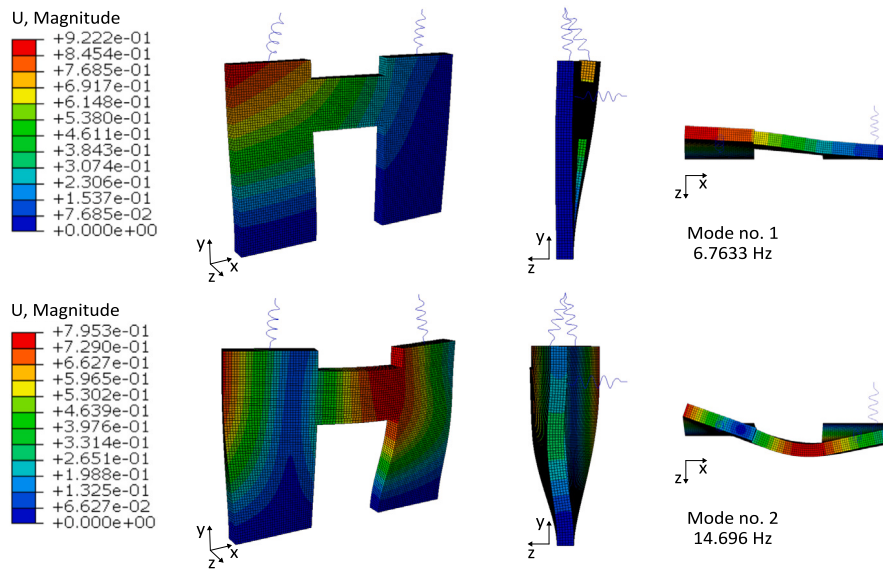


Fig. 7. First and second modes of vibration of the numerical model of Specimen A (U, Magnitude denotes the resultant displacement variable).

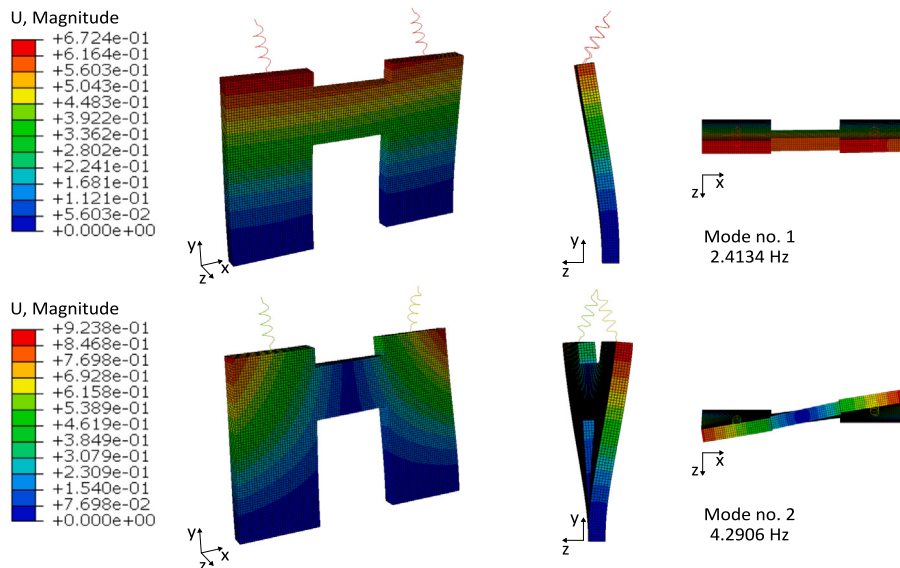


Fig. 8. First and second modes of vibration of the numerical model of Specimen B (U, Magnitude denotes the resultant displacement variable).

D1 and S1, respectively. Overall, the mode shapes identified for both wall systems are characterized by low modal complexity, as confirmed by MPC values consistently exceeding 85%. The identified modal signatures in both wall systems are similar, with modal shapes primarily involving bending around the z-axis. However, some discrepancies are noticeable due to the different magnitudes of the applied dead loads and the distinct restraint conditions. For example, the fundamental frequency of Specimen A is 6.779 Hz, while Specimen B exhibits a frequency of 2.467 Hz. The higher magnitude of the dead loads applied on Specimen A contributed to making this wall system more rigid than Specimen B. The connection to the actuator however played an important role in making Specimen A stiffer than Specimen B, as evident when comparing the main identified mode shapes. Specifically, because of the connection to the actuator, the right pier of Specimen A displays limited movements in the out-of-plane direction compared to the unrestrained left pier and the piers of Specimen B. Similar considerations can be drawn for the other vibration modes.

Figs. 7 and 8 show the reference modal features obtained by linear perturbation analyses of the numerical models of Specimens A and B,

respectively. Overall, after proper calibration both numerical models successfully reproduced the first and second modes of vibration that dominate the dynamic response of the case study structures. In the case of Specimen A, the model was able to replicate the fundamental frequency and the corresponding mode shape with a relative error of 0.23% and a MAC value against the experimental mode of 1.00, respectively. For the second mode of vibration, a relative error in frequency of 1.22% and a MAC value of 0.80 were determined. For Specimen B, the comparison between the experimental and numerical modal features yielded a relative error in frequency of 2.12% and a MAC value of 0.97 for the first mode of vibration. Similarly, for the second mode of vibration, a relative error in frequency of -2.52% and a MAC value of 0.95 were found. In both specimens, even after proper calibration, the numerical models were unable to reproduce higher-order modes identified experimentally (i.e., modes No. 3, 4, etc.). This can be attributed to the fact that the interactions among the wall systems, the hydraulic jacks, and the actuator, were reproduced by means of linear elastic axial springs in the numerical simulations, whereas

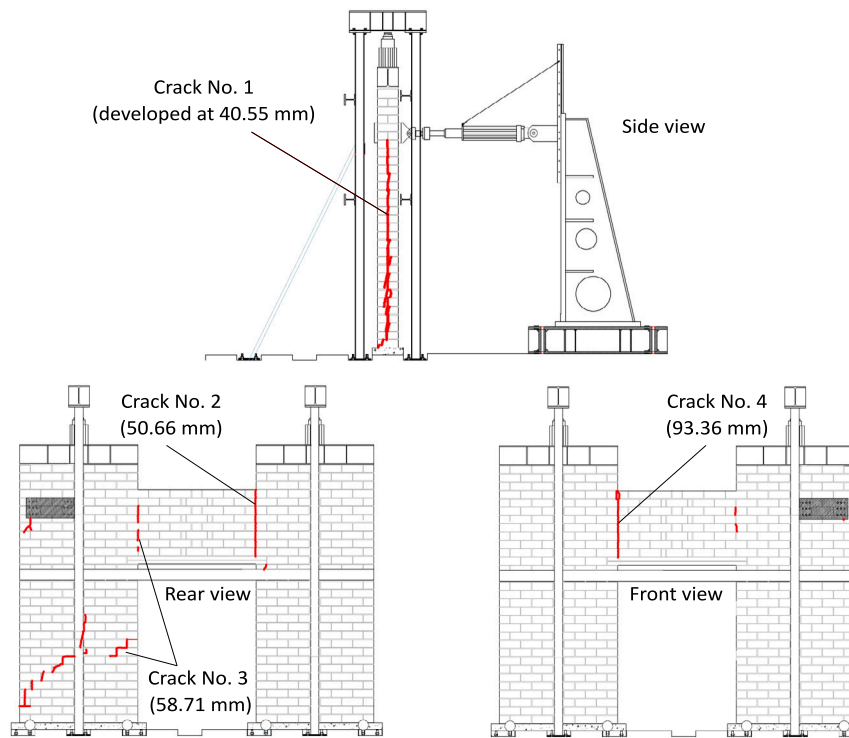


Fig. 9. Cracking pattern observed experimentally on Specimen A by imposing increasing out-of-plane displacements to the right pier.

these parts likely exhibit non-linear interactions in the experimental settings.

#### 4.2. Cracking patterns

Fig. 9 illustrates the experimental cracking pattern found in Specimen A as the applied eccentric out-of-plane displacements increased. No visible cracks were observed on the structure until test step D6. The first crack, referred to as crack No. 1, appeared across the thickness of the right part of the wall system at an out-of-plane displacement value of 40.55 mm (corresponding to out-of-plane drift ratio of 1.31% and an out-of-plane force of 39.00 kN). The crack extended almost the full height of the specimen, although its opening was not significant. As the out-of-plane displacement was further increased, new cracks developed in the specimen (cracks No. 2 and No. 3 at out-of-plane displacements of 51.00 mm and 59.00 mm, respectively, corresponding to an out-of-plane drift ratio of 1.65% and 1.90%), while the existing cracks widened. The out-of-plane peak force of 41.65 kN was reached at an out-of-plane displacement of 58.00 mm (i.e., at an out-of-plane drift ratio of 1.87%). At this stage, the wall system still retained some load-bearing capacity, so the out-of-plane displacement was further increased until crack No. 4 developed. In this case, the out-of-plane displacement reached 93.36 mm (i.e., an out-of-plane drift ratio of 3.01%), corresponding to an out-of-plane residual force of 19.90 kN. Fig. 10 shows the cracking pattern that developed on Specimen B as the settlement imposed on its movable foundation increased. No visible cracks were found until the settlement reached 9.00 mm (step S3, corresponding to an in-plane drift ratio of 0.26%). At this point, cracks appeared at the end portions of the spandrel panel. These cracks widened and deepened as the settlement was further increased to 15.00 mm (step S4, i.e., at an in-plane drift ratio of 0.44%) and 35.00 mm (step S5, corresponding to an in-plane drift ratio of 1.03%), without the development of new cracks.

Fig. 11 depicts the damage pattern predicted by the numerical model of Specimen A. Overall, the obtained experimental and numerical cracking patterns are consistent with each other, although damages

in the numerical model appeared slightly earlier compared to the experiments. The crack along the thickness of the right side of the wall system began to develop on the numerical model from test step D5. At this stage, the entity of this damage was minimal, reaching its maximum severity at step D6. Further damages can be observed on the numerical model at step D5, located near the ends of the spandrel panel and in the lower part of the base of the pier connected to the actuator. These damages started developing in the numerical model at test step D2 and continued to expand until step D6. On the other hand, Fig. 12 shows the damage pattern estimated by the numerical model of Specimen B. Similarly, there is good consistency between the experimental and numerical cracking patterns. Damages started to develop at the lateral edges of the spandrel in the numerical model at test step S3. At this stage, the extent of the numerically predicted damage exceeds that observed experimentally in the specimen. As it was also observed during the experiment, the damage predicted by the model increases as the differential settlement imposed on the left pier increases in magnitude.

#### 4.3. Damage effects on modal features of specimens

Fig. 13 illustrates the decay observed in the experimental modal features of Specimen A due to the imposed progressive damage. The drift ratio values calculated for each damage step are also noted in the graph to provide a distinct definition of the damage measure, which can be used to make evaluations/correlations in other structures with different size. Overall, the reported trends indicate that the changes in terms of natural frequencies and MAC values clearly reflect the progressive damage to the wall system as the applied out-of-plane displacements increased. Interestingly, the modal features exhibited changes even when the tested structure showed no visible damage. The decay of the natural frequencies occurred with a fairly linear trend, with modes No. 4 and 5 exhibiting the largest decreases in frequency value (around  $-12\%$  and  $-20\%$  at the load peak, respectively). In particular, mode No. 5 suffered an abrupt drop in its frequency due to the opening of the first cracks (cracks No. 1 and 2). The MAC values

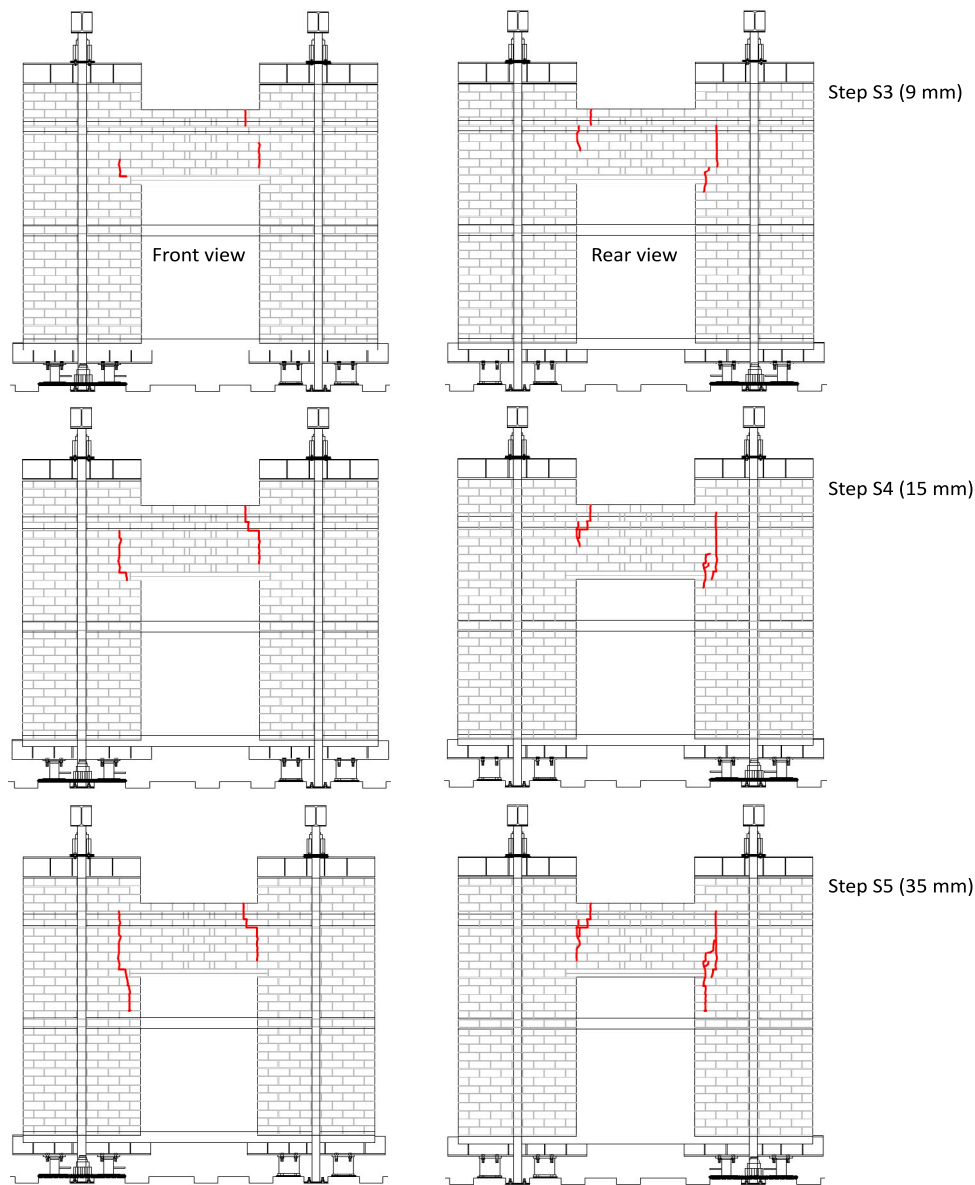


Fig. 10. Cracking pattern observed experimentally on Specimen B by imposing increasing differential settlements at the foundation of the left pier.

of all the identified modes of vibration decreased slightly between steps D2 and D3 of the test sequence. Nonetheless, a significant decay of the MAC value can be seen from step D4 onwards for all mode shapes, with the exception of modes No. 1 and 2, the MAC values of which remained fairly stable up to the peak condition. This indicates that the corresponding mode shapes were not very sensitive to the progressive structural damage. The greatest changes in the mode shapes with respect to reference values can be observed for mode No. 3. This is likely because its modal shape consisted of a double bending of the wall around both the  $x$ - and  $z$ -axes. An anomalous trend of the MAC value can be observed for mode No. 5 between steps D5 and D6 of the test sequence. In fact, the MAC value of this vibration mode increased between steps D5 and D6 as the damage state of the wall system grew. This unexpected result may be attributed to limitations in the number of monitoring sensors or to errors in the dynamic identification due to low ambient excitation to which the wall system was exposed during AVTs.

In the case of Specimen B under increasing differential foundation settlements, a clear sensitivity of the experimental modal features to progressive structural damage was also observed as depicted in Fig. 14.

In this case, only modes No. 2 and 4 exhibited significant decays in terms of frequencies before crack initiation (i.e., after the execution of step S2, with changes in natural frequencies less than  $-2.5\%$ ). From step S3 onwards, the resonant frequencies of modes No. 2, 3, 5, and 7 exhibited a gradual linear decay, while modes No. 4 and 6 experienced a sharp decrease. Notably, mode No. 6 suffered the largest decrease, with a decay of about  $-14\%$  at crack initiation, eventually reaching a decay of  $-27\%$  at the end of the test sequence (step S5). The resonant frequency associated with mode No. 8 appeared less sensitive to the developed cracking pattern, as it only underwent small changes at crack initiation (max  $-1.00\%$  at step S3). Note in Fig. 14(a) that an unexpected increasing trend was observed in the resonance frequency of mode No. 1 under progressive damage. This behavior, unlikely to result from material stiffening due to the progressive crack opening, can only be attributed to potential variations in the stiffness of the wall induced by modifications in the structural setting. In fact, in the experimental setup, differential settlements were simulated by progressively reducing the initial height of the hand-operated steel mechanism placed under the basement of the left pier of Specimen B, which may have induced some stiffening of the wall and the subsequent increase in the

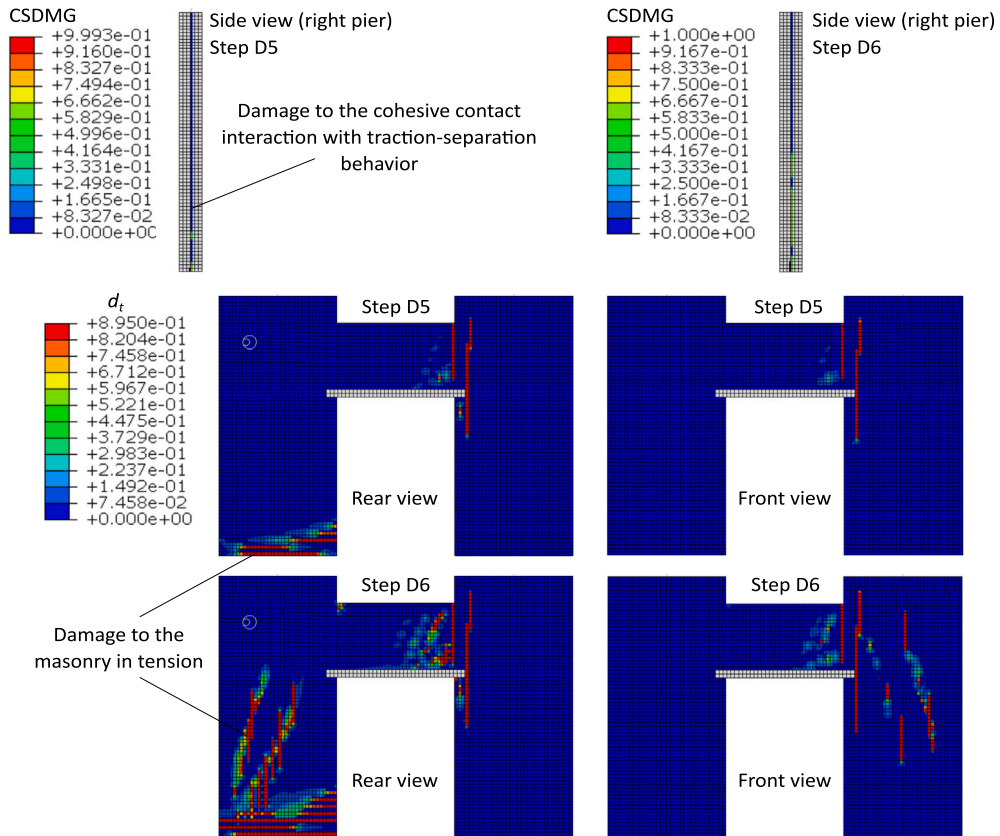


Fig. 11. Numerical simulation of the cracking pattern developed on Specimen A (CSDMG denotes the damage parameter related to the cohesive contact, while  $d_t$  is the tensile damage variable related to the masonry).

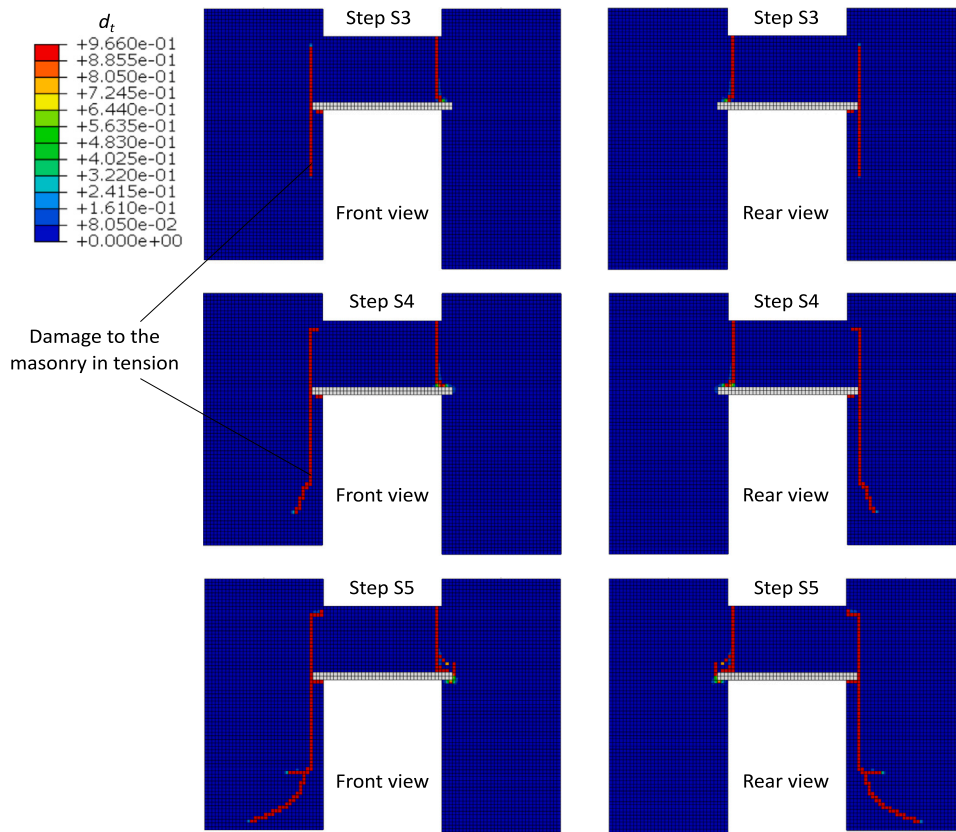


Fig. 12. Numerical simulation of the cracking pattern developed on Specimen B ( $d_t$  is the tensile damage variable related to the masonry).

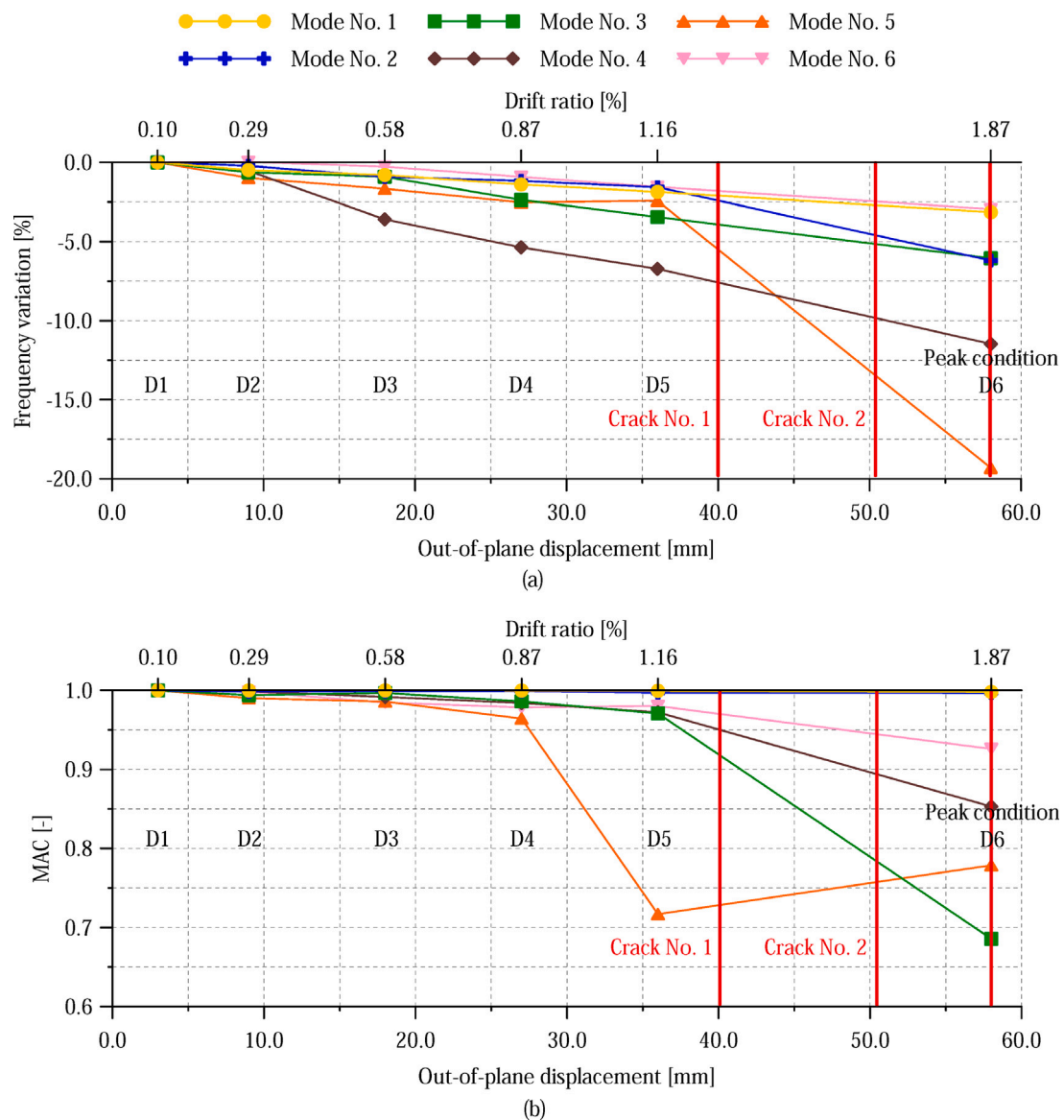


Fig. 13. Changes in the experimental modal features of Specimen A due to the imposed progressive damage: (a) relative variations in natural frequencies, and (b) MAC values against the healthy baseline.

fundamental frequency. When examining the MAC values in Fig. 14(b), it is noticeable that almost all the modes experienced modifications due to the progressive damage, except for modes No. 1 and 2, which exhibited less sensitivity. The decline of the MAC values occurred with an approximately linear trend for modes No. 3, 5, 7, and 8. Nevertheless, similar to the results in Fig. 14(a), anomalous trends in the MAC values of modes No. 4 and 6 were found between steps S4 and S5 of the test sequence. It is interesting to note that these modes were the most sensitive to progressive damage in terms of natural frequencies, as observed for mode No. 5 of Specimen A. These modes share an unexpected response of the MAC index to the increase in crack opening, which may be attributed to the factors mentioned earlier.

Figs. 15 and 16 illustrate the comparison between the experimental and numerically determined decays for the first two modes of vibration of Specimens A and B, respectively. Overall, it is clear that the developed numerical models, after proper calibration, are capable of reproducing the global trends in the damage-induced variations on the modal signatures of the wall systems, achieving close fits with the experimental results. Only some noticeable discrepancies are found for the fundamental frequency of Specimen B, due to the fact that

the numerical model was unable to simulate the stiffening effects that affected this mode of vibration in the experimental setting.

#### 4.4. Structural integrity assessment

Fig. 17(a) shows the force–displacement curve resulting from the execution of the tests carried out on Specimen A, with inserts indicating the seismic limit states prescribed by the Italian Building Code. In this figure, the OLS was associated with the end of the linear elastic range of the wall system, while the DLLS was set at the formation of the first visible crack on the tested structure. The LSLS was associated with the first marked reduction in the load-bearing capacity of the specimen against the out-of-plane displacement, while the CLS was established when a small margin of safety against out-of-plane collapse mechanisms was reached. Among the SLSs and ULSS, DLLS and LSLS were considered the most significant limits. Accordingly, Fig. 17(b) illustrates the decay of natural frequencies and the MAC values estimated at DLLS and LSLS. Overall, all the modes of vibration demonstrated a certain sensitivity to the considered limit states when assessing the relative variations in the natural frequencies, while only a few modes showed comparable

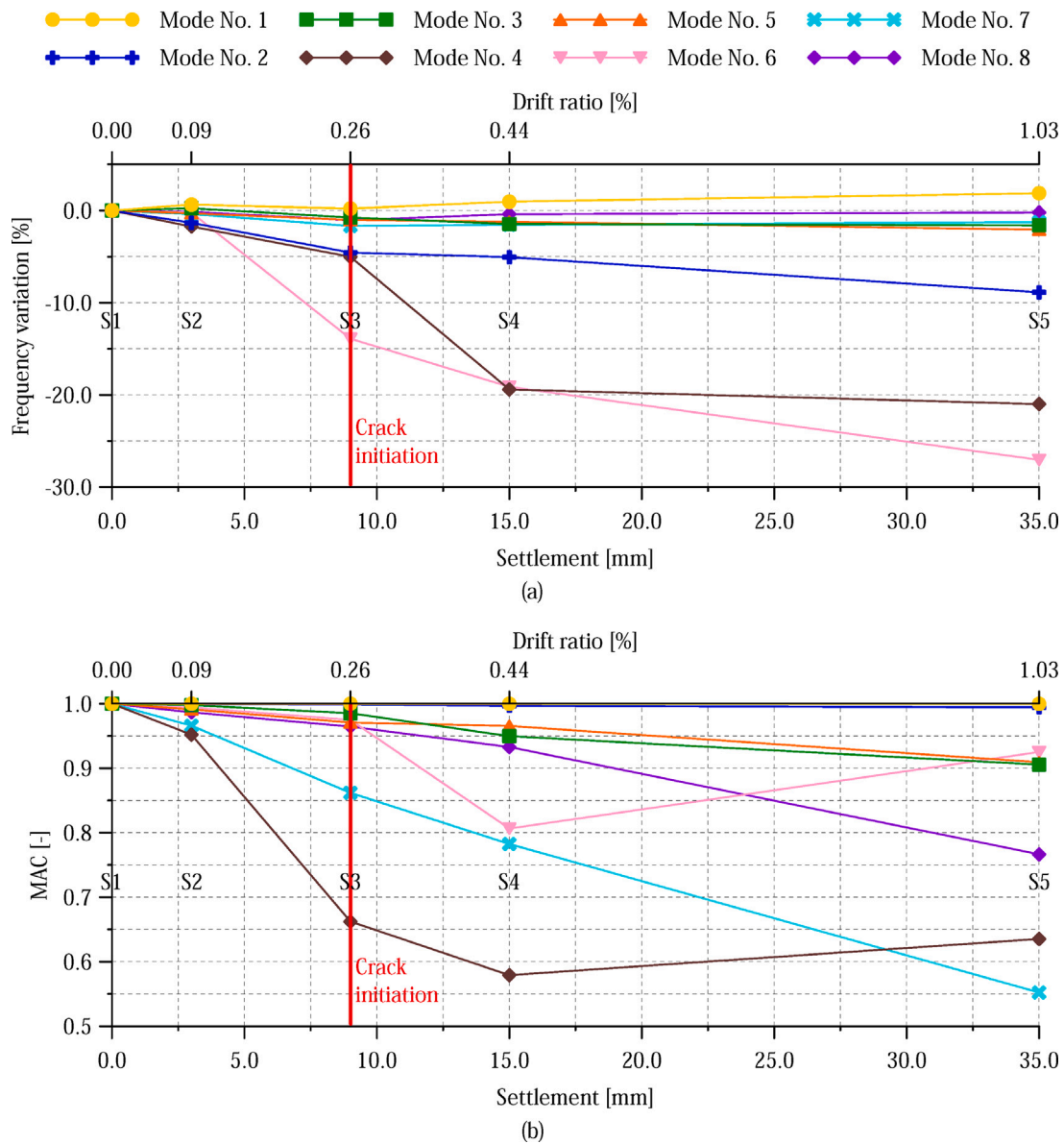


Fig. 14. Changes in the experimental modal features of Specimen B due to the imposed progressive damage: (a) relative variations in natural frequencies, and (b) MAC values against the healthy baseline.

sensitivity in terms of changes in their mode shapes. The minimum relative variation in frequency at DLLS was computed for mode No. 6, with a value of  $-1.78\%$ , while the maximum value was found for mode No. 4 with a variation of about  $-7.5\%$ . On average, a mean frequency decay of about  $-3.4\%$  was determined at DLLS, excluding the maximum and minimum values. The most sensitive mode shape at DLLS was that of mode No. 5, for which a MAC value equal to 0.73 was obtained. The other modes of vibration exhibited MAC values ranging between 1.00 and 0.91, thus demonstrating limited sensitivity against this limit state. When achieving the LSLS, the relative variations in frequency increased significantly, finding a minimum value of  $-2.95\%$  for mode No. 6, and a maximum value of  $-20\%$  for mode No. 5. In this case, the average frequency decay was about  $-6.71\%$ , excluding the maximum and minimum values. In terms of mode shapes, the most sensitive mode was mode No. 3, which was characterized by a MAC value of 0.69. The MAC index remained above 0.85 for the other vibration modes, except for mode No. 5, for which a MAC value of 0.78 was determined at LSLS, and thus slightly above the MAC value determined at DLLS (0.73). As discussed in Section 4.3, this anomalous

trend may be justified by practical limitations of the adopted OMA technique.

The structural assessment results obtained for Specimen B are reported in Fig. 18. It should be noted that mode No. 1 was excluded from this evaluation, given the anomalous damage-induced effects previously discussed. The decays in the modal features of the modes of vibration included in the assessment were interpolated from the decay trends reported in Section 4.3, by considering the limit foundational settlements of 6.80 mm (corresponding to the achievement of SLS) and of 22.67 mm (ULS) as shown in Fig. 18(a). Fig. 18(b) reports the decays in the natural frequencies and the MAC values estimated at SLS and ULS. At SLS, mode No. 3 exhibited the minimum frequency decay ( $-0.39\%$ ), while the maximum value was determined for mode No. 6 ( $-8.88\%$ ). The average decay in frequency was about  $-1.96\%$ , without considering the maximum and minimum values. In terms of mode shapes, only mode No. 4 exhibited a significant sensitivity to damage, with a MAC value equal to 0.77. The remaining vibration modes were characterized by MAC values between 0.90 and 0.99, indicating a poor sensitivity to the damage level at SLS. Nonetheless, when achieving the ULS, marked modifications in the natural frequencies of the wall were

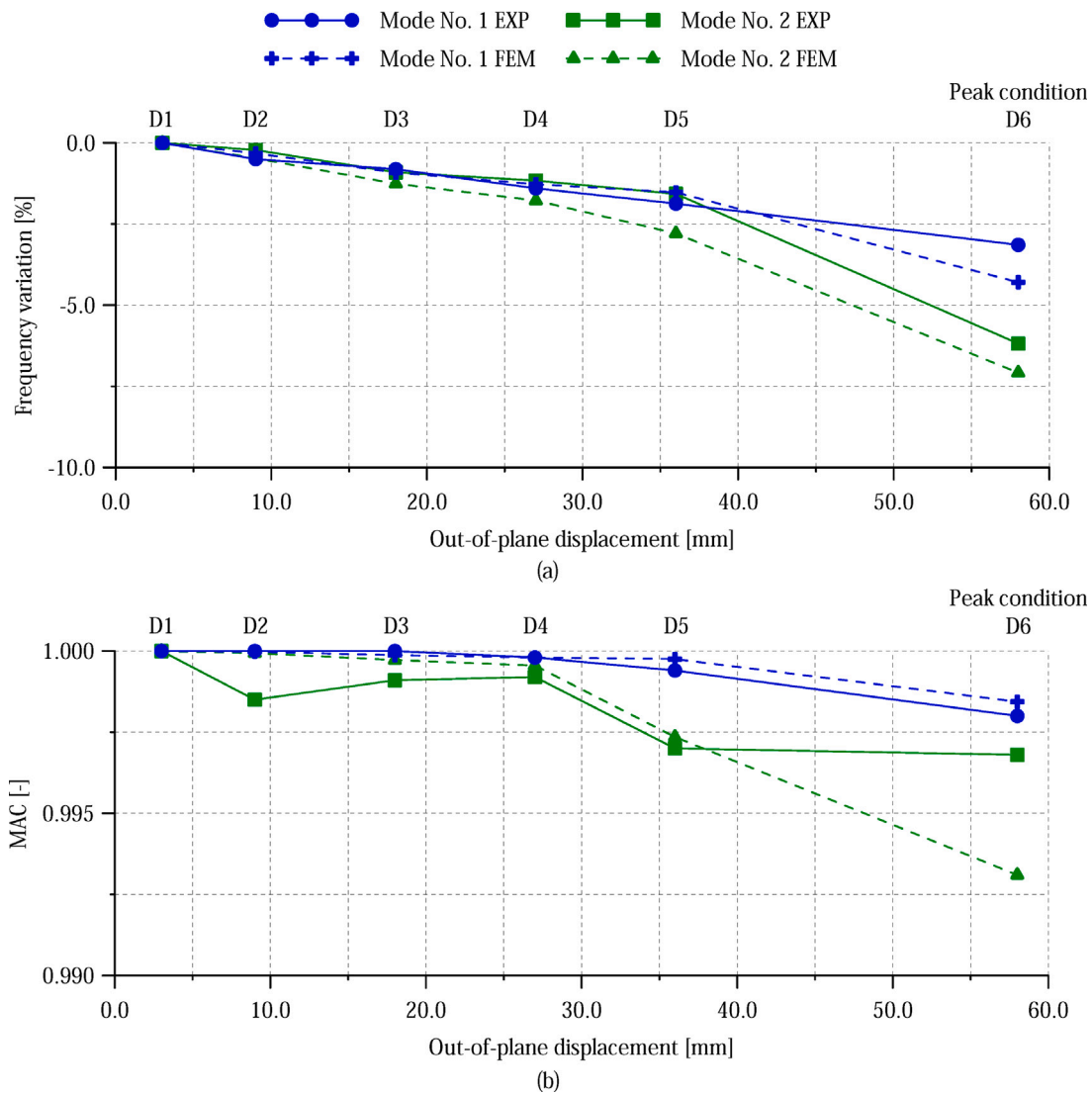


Fig. 15. Comparison between the experimental and numerical decays obtained for the modal features specializing the first and second modes of vibration of Specimen A: (a) relative variations in natural frequencies, and (b) MAC values against the healthy baseline.

found. The minimum relative variation in frequency, equal to  $-0.32\%$ , was calculated for mode No. 8. It should be noted that, at SLS, the frequency decay of mode No. 8 was about  $-0.70\%$ , which, compared to the decay determined at SLS, highlights an anomalous trend. However, considering the high value of the frequency of this mode of vibration (above 40 Hz), such an anomalous trend may be attributed to a low excitation of this mode and limitations in the adopted OMA approach. The maximum relative variation in frequency of  $-22\%$  was computed for mode No. 6. The average decay in frequency at ULS, excluding the maximum and minimum values, was about  $-6.18\%$ . The maximum sensitivity in terms of MAC values at ULS was found for modes No. 4 (0.60) and No. 7 (0.69), while the remaining modes exhibited only moderate sensitivities with MAC values ranging between 0.85 and 0.99.

### 5. Conclusions

This work has presented a numerical and experimental program aimed at investigating the impact of damage in masonry wall systems on their modal properties and the correlation with their load-bearing capacity. The presented investigation has filled some current research gaps by consistently demonstrating the sensitivity of both natural frequencies and mode shapes to localized/small structural damage,

proposing correlations between decays in modal features and performance limit states, and then corroborating the use of numerical models for reproducing damage-induced decays in both vibration frequencies and mode shapes.

Two full-scale masonry wall systems made of tuff stones and mortar layers were tested under laboratory-controlled progressive damage. The first wall system (Specimen A) was progressively damaged by applying increasing out-of-plane displacements to its right pier, while the second system (Specimen B) was subjected to differential foundation settlements. Both specimens were instrumented with a dense network of high-sensitivity piezoelectric accelerometers, with the purpose of conducting AVTs between every incremental damage state. Correlations between the damage-induced decays in the modal features and residual load-bearing capacity were assessed for both tested structures. In particular, the seismic limit states provided by the Italian Building Code and the geotechnical limit states included in Eurocode 7 were adopted to evaluate reductions in the load-bearing capacity of Specimens A and B, respectively. Subsequently, the attainment of each limit state was associated with the corresponding decay of natural frequencies/MAC values, thereby accomplishing a vibration-based assessment of the structural integrity of the wall systems. Non-linear FE models were developed to numerically simulate the experiments and interpret the dynamic identification results. After reproducing every damage

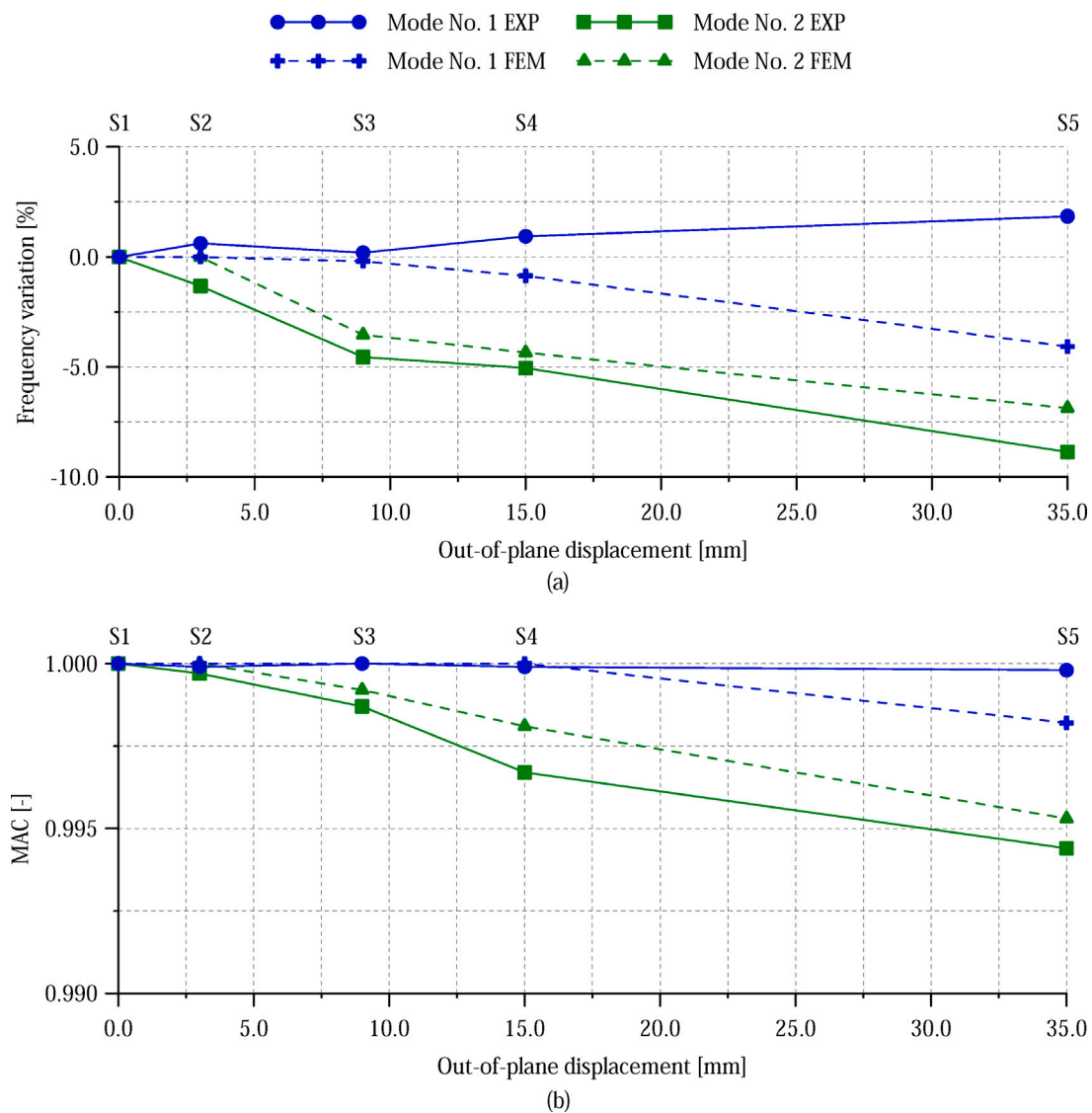


Fig. 16. Comparison between the experimental and numerical decays obtained for the modal features specializing the first and second modes of vibration of Specimen B: (a) relative variations in natural frequencies, and (b) MAC values against the healthy baseline.

state in the experimental sequence, a linear perturbation analysis was carried out to determine the modal features specializing the dynamic response of the numerical models by considering the tangent stiffness matrix. The FE models, after proper calibration, successfully replicated the experimentally observed cracking pattern, resulting in a close fit between the experimental and numerical decays in the modal features of the wall systems.

Six and eight modes of vibration were experimentally determined for Specimens A and B, respectively. The corresponding natural frequencies were identified as clear peaks in the singular values of the spectral density matrices, and their mode shapes were characterized by low modal complexity. Overall, the results from the dynamic identifications performed at each step of damage were consistent. Only a limited number of modes exhibited unexpected stiffening effects, which may be conceivably explained by non-linear interactions with the supports, and/or variations in the constraint conditions during the testing sequences. These phenomena are typical of laboratory testing and do not affect the overall reliability of the results. The damage detection analyses comparing the modal signatures with the crack openings indicated a clear sensitivity to damage by both natural frequencies and mode shapes. Notably, significant decays in the modal features were

observed even for damage states of low severity, not observable by visual inspections. The outcomes from the structural integrity assessment pointed out that even slight reductions in the load-bearing capacity of the wall systems, corresponding to the SLSs, resulted in substantial modifications of the natural frequencies compared to their reference (healthy) values. Specifically, for Specimen A, an average decay of the natural frequencies of  $-3.4\%$  (excluding maximum and minimum values) was computed at DLLS, which corresponded to the formation of the first cracks on the wall system. Similarly, an average frequency decay of  $-1.96\%$  (excluding maximum and minimum decays) was calculated for Specimen B at SLS, with a settlement of the left basement of the wall system of  $6.80$  mm (no visible cracks were detected on Specimen B at this stage). On the other hand, in both testing specimens, only a few modes exhibited significant decays in the MAC value at SLSs, e.g., below  $0.80$ . While mode shapes exhibit lower sensitivity to damage when compared to natural frequencies, it is noteworthy that some changes in mode shapes were already observed at the initial stages of crack development. It is however important to emphasize that in real SHM applications the heightened sensitivity of natural frequencies to structural damage is counterbalanced by their increased susceptibility to environmental fluctuations, including temperature and humidity. In contrast, mode shapes are recognized for their relatively minor susceptibility to such external factors.

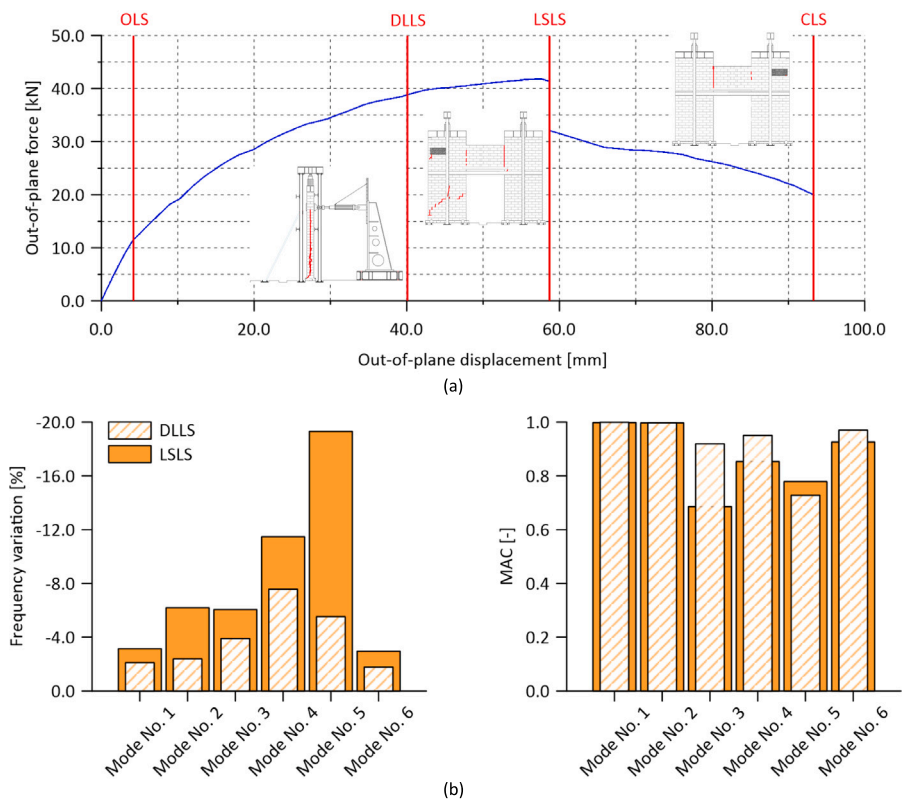


Fig. 17. Structural integrity assessment of Specimen A: (a) force–displacement curve with inserts reporting the seismic limit states provided by the Italian Building Code; (b) relative variations in natural frequencies and MAC values estimated at the Damage Limitation Limit State (DLLS) and Life Safety Limit State (LSLS).

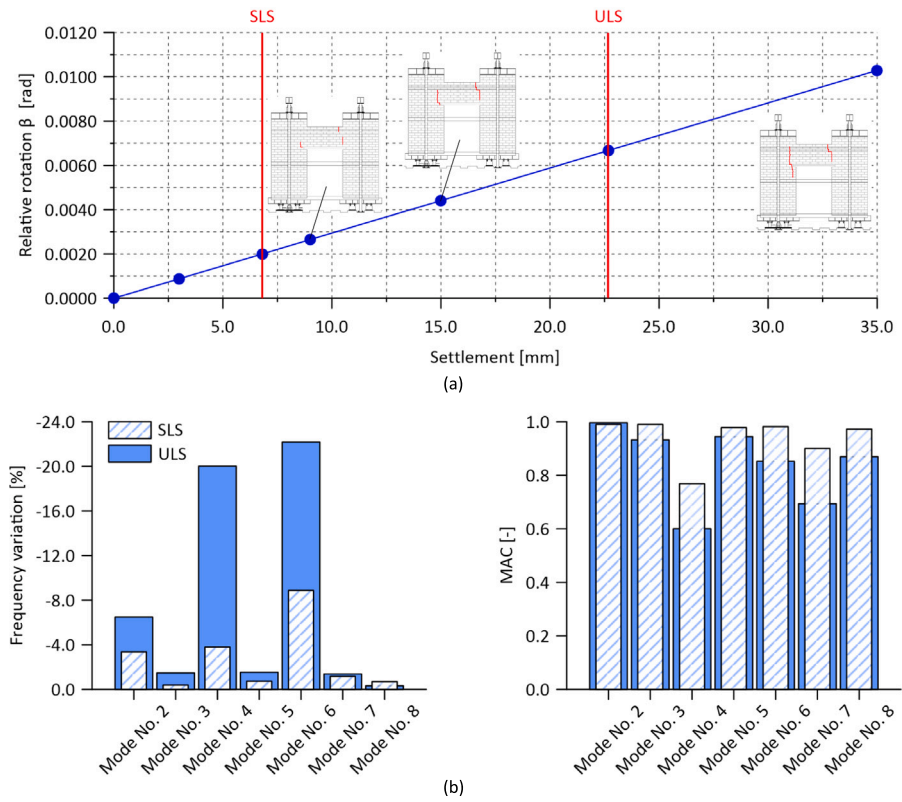


Fig. 18. Structural integrity assessment of Specimen B: (a) relative rotations versus settlements of the foundation system with inserts reporting the geotechnical limit states provided by Eurocode 7; (b) relative variations in natural frequencies and MAC values estimated at the Serviceability Limit State (SLS) and Ultimate Limit State (ULS).

Overall, the results presented in this study corroborate the feasibility of using modal features for detecting relatively small structural damages to historical masonry buildings. This insight is further supported by the results obtained by evaluating the structural performance of the studied wall specimens, which was made possible by pairing decays of modal features and structural limit states. The correlations found in this work between decays in modal features and performance limit states can be used as reference in further experiments. However, although such correlations were derived from laboratory testing of full-scale masonry wall specimens subjected to controlled damage conditions, they can also provide a basis for making preliminary assessments in the case of real SHM applications involving masonry structures under similar structural failures. The results presented in this work also highlight that the use of properly calibrated non-linear FE models can accurately replicate damage-induced modifications in both vibration frequencies and mode shapes. Therefore, the use of model-based damage identification approaches combined with OMA seems to be fully justified in the case of masonry structures. Future studies should focus on corroborating the use of OMA methods for SHM of masonry structures under changing environmental conditions. To this end, continuous SHM field applications involving full-scale masonry building specimens subjected to controlled damage under changing temperature and humidity conditions are especially needed. In this context, new SHM strategies should be proposed that use a limited amount of data to train compensation algorithms for the removal of environmental effects from modal features tracked over time, thus overcoming one of the main drawbacks encountered in continuous vibration-based SHM applications, that is, the collection of large data sets for proper calibration of statistical pattern recognition models.

#### CRedit authorship contribution statement

**Andrea Meoni:** Writing – review & editing, Writing – original draft, Visualization, Validation, Software, Methodology, Investigation, Formal analysis, Data curation, Conceptualization. **Antonella D’Alessandro:** Writing – review & editing, Investigation, Conceptualization. **Michele Mattiacci:** Writing – review & editing, Software, Investigation, Data curation. **Enrique García-Macías:** Writing – review & editing, Software. **Felice Saviano:** Writing – review & editing, Investigation. **Fulvio Parisi:** Writing – review & editing, Supervision, Methodology, Investigation. **Gian Piero Lignola:** Writing – review & editing, Supervision, Methodology, Investigation, Funding acquisition. **Filippo Ubertini:** Writing – review & editing, Supervision, Methodology, Investigation, Funding acquisition, Conceptualization.

#### Declaration of competing interest

The authors declare that they have no known competing financial interests or personal relationships that could have appeared to influence the work reported in this paper.

#### Data availability

Data will be made available on request.

#### Acknowledgments

This work was financially supported by the Italian Ministry of University and Research (MUR) through the PRIN-2017 project DETECT-AGING (Degradation Effects on sTructural safEty of Cultural herITAGE constructions through simulation and health monitoriNG, Project code 201747Y73L). The first Author also acknowledges the European Union - NextGenerationEU and the University of Perugia for supporting the work through the project Vitality framed within the National Innovation Ecosystem Grant ECS00000041.

#### References

- [1] Bosiljkov V, Uranjek M, Žarnić R, Bokan-Bosiljkov V. An integrated diagnostic approach for the assessment of historic masonry structures. *J Cult Herit* 2010;11(3):239–49.
- [2] Parisi F, Augenti N. Uncertainty in seismic capacity of masonry buildings. *Buildings* 2012;2(3):218–30.
- [3] Giamundo V, Sarhosis V, Lignola G, Sheng Y, Manfredi G. Evaluation of different computational modelling strategies for the analysis of low strength masonry structures. *Eng Struct* 2014;73:160–9.
- [4] Augenti N, Parisi F. Teoria e tecnica delle strutture in muratura: analisi e progettazione. HOEPLI EDITORE; 2019.
- [5] Pulatsu B, Gonen S, Parisi F, Erdogmus E, Tuncay K, Funari MF, Lourenço PB. Probabilistic approach to assess URM walls with openings using discrete rigid block analysis (D-RBA). *J Build Eng* 2022;61:105269.
- [6] Pulatsu B, Gonen S, Funari MF, Parisi F. Spatial stochastic D-RBA and limit equilibrium analysis of unreinforced masonry pier-spandrel structures. *Eng Struct* 2023;296:116897.
- [7] Portioli F, Cascini L. Assessment of masonry structures subjected to foundation settlements using rigid block limit analysis. *Eng Struct* 2016;113:347–61.
- [8] D’Altri AM, Castellazzi G, de Miranda S, Tralli A. Seismic-induced damage in historical masonry vaults: A case-study in the 2012 Emilia earthquake-stricken area. *J Build Eng* 2017;13:224–43.
- [9] Sarhosis V, Milani G, Formisano A, Fabbrocino F. Evaluation of different approaches for the estimation of the seismic vulnerability of masonry towers. *Bull Earthq Eng* 2018;16:1511–45.
- [10] Clementi F, Ferrante A, Giordano E, Dubois F, Lenci S. Damage assessment of ancient masonry churches stroked by the Central Italy earthquakes of 2016 by the non-smooth contact dynamics method. *Bull Earthq Eng* 2020;18:455–86.
- [11] Sivori D, Cattari S, Lepidi M. A methodological framework to relate the earthquake-induced frequency reduction to structural damage in masonry buildings. *Bull Earthq Eng* 2022;9(9):4603–38.
- [12] Saviano F, Parisi F, Lignola GP. Material aging effects on the in-plane lateral capacity of tuff stone masonry walls: a numerical investigation. *Mater Struct* 2022;55(7):198.
- [13] Bennati S, Nardini L, Salvatore W. Dynamic behavior of a medieval masonry bell tower. II: Measurement and modeling of the tower motion. *J Struct Eng* 2005;131(11):1656–64.
- [14] Ivorra S, Pallarés FJ. Dynamic investigations on a masonry bell tower. *Eng Struct* 2006;28(5):660–7.
- [15] Aras F, Krstevska L, Altay G, Tashkov L. Experimental and numerical modal analyses of a historical masonry palace. *Constr Build Mater* 2011;25(1):81–91.
- [16] Masciotta M-G, Ramos LF, Lourenço PB. The importance of structural monitoring as a diagnosis and control tool in the restoration process of heritage structures: A case study in Portugal. *J Cult Herit* 2017;27:36–47.
- [17] Ferrante A, Clementi F, Milani G. Dynamic behavior of an inclined existing masonry tower in Italy. *Front Built Environ* 2019;5:33.
- [18] García-Macías E, Ubertini F. Automated operational modal analysis and ambient noise deconvolution interferometry for the full structural identification of historic towers: A case study of the Sciri Tower in Perugia, Italy. *Eng Struct* 2020;215:110615.
- [19] Pallarés FJ, Betti M, Bartoli G, Pallarés L. Structural health monitoring (SHM) and Nondestructive testing (NDT) of slender masonry structures: A practical review. *Constr Build Mater* 2021;297:123768.
- [20] Foti D, Ivorra S, Sabbà MF, et al. Dynamic investigation of an ancient masonry bell tower with operational modal analysis: A non-destructive experimental technique to obtain the dynamic characteristics of a structure. *The Open Construct Build Technol J* 2012.
- [21] Ramos LF, Aguilar R, Lourenço PB, Moreira S. Dynamic structural health monitoring of Saint Torcato church. *Mech Syst Signal Process* 2013;35(1–2):1–15.
- [22] Giamundo V, Lignola G, Maddaloni G, Da Porto F, Prota A, Manfredi G. Shaking table tests on a full-scale unreinforced and IMG-retrofitted clay brick masonry barrel vault. *Bull Earthq Eng* 2016;14:1663–93.
- [23] Gentile C, Guidobaldi M, Saisi A. One-year dynamic monitoring of a historic tower: damage detection under changing environment. *Meccanica* 2016;51:2873–89.
- [24] Ubertini F, Comanducci G, Cavalagli N. Vibration-based structural health monitoring of a historic bell-tower using output-only measurements and multivariate statistical analysis. *Struct Health Monit* 2016;15(4):438–57.
- [25] Ramaglia G, Lignola GP, Balsamo A, Prota A, Manfredi G. Seismic strengthening of masonry vaults with abutments using textile-reinforced mortar. *J Compos Construct* 2017;21(2):04016079.
- [26] Ubertini F, Cavalagli N, Kita A, Comanducci G. Assessment of a monumental masonry bell-tower after 2016 Central Italy seismic sequence by long-term SHM. *Bull Earthq Eng* 2018;16:775–801.
- [27] Gentile C, Ruccolo A, Canali F. Long-term monitoring for the condition-based structural maintenance of the Milan Cathedral. *Constr Build Mater* 2019;228:117101.
- [28] Barsocchi P, Bartoli G, Betti M, Girardi M, Mammolito S, Pellegrini D, Zini G. Wireless sensor networks for continuous structural health monitoring of historic masonry towers. *Int J Architect Herit* 2021;15(1):22–44.

- [29] Sun Q, Rainieri C, Ren W, Yan W, Fabbrocino G. Automated operational modal analysis of bell towers subjected to narrowband input. *Structures* 2023;54:78–88.
- [30] Cross EJ, Worden K, Chen Q. Cointegration: a novel approach for the removal of environmental trends in structural health monitoring data. *Proc R Soc A: Math Phys Eng Sci* 2011;467(2133):2712–32.
- [31] Bellino A, Fasana A, Garibaldi L, Marchesiello S. PCA-based detection of damage in time-varying systems. *Mech Syst Signal Process* 2010;24(7):2250–60.
- [32] Cavalagli N, Comanducci G, Gentile C, Guidobaldi M, Saisi A, Ubertini F. Detecting earthquake-induced damage in historic masonry towers using continuously monitored dynamic response-only data. *Proc Eng* 2017;199:3416–21.
- [33] Civera M, Calamai G, Zanotti Fragonara L. System identification via fast relaxed vector fitting for the structural health monitoring of masonry bridges. *Structures* 2021;30:277–93.
- [34] Masciotta MG, Pellegrini D. Tracking the variation of complex mode shapes for damage quantification and localization in structural systems. *Mech Syst Signal Process* 2022;169:108731.
- [35] Kouris LAS, Penna A, Magenes G. Dynamic modification and damage propagation of a two-storey full-scale masonry building. *Adv Civ Eng* 2019;2019.
- [36] Pepi C, Cavalagli N, Gusella V, Gioffre M. Damage detection via modal analysis of masonry structures using shaking table tests. *Earthq Eng Struct Dynam* 2021;50(8):2077–97.
- [37] Kaya A, Adanur S, Bello RA, Genç AF, Okur FY, Sunca F, Günaydin M, Altunışık AC, Sevim B. Post-earthquake damage assessments of unreinforced masonry (URM) buildings by shake table test and numerical visualization. *Eng Fail Anal* 2023;143:106858.
- [38] Ramos LF, De Roeck G, Lourenço PB, Campos-Costa A. Damage identification on arched masonry structures using ambient and random impact vibrations. *Eng Struct* 2010;32(1):146–62.
- [39] Oyarzo-Vera C, Chouh N, et al. Damage identification of unreinforced masonry panels using vibration-based techniques. *Shock Vib* 2017;2017.
- [40] Boscato G, Recchia E, Cecchi A. Non-destructive experimentation: Dynamic identification of multi-leaf masonry walls damaged and consolidated. *Composites B* 2018;133:145–65.
- [41] Giordano E, Mendes N, Masciotta MG, Clementi F, Sadeghi NH, Silva RA, Oliveira DV. Expeditious damage index for arched structures based on dynamic identification testing. *Constr Build Mater* 2020;265:120236.
- [42] Castellano A, Camassa D, Fraddosio A, Scacco J, Piccioni MD, Milani G. Dynamic damage identification for a full-scale parabolic tuff barrel vault under differential settlements of the supports. *Constr Build Mater* 2021;291:123271.
- [43] Furtado A, Rodrigues H, Arêde A, Varum H. Modal identification of infill masonry walls with different characteristics. *Eng Struct* 2017;145:118–34.
- [44] Nicoletti V, Arezzo D, Carbonari S, Gara F. Vibration-based tests and results for the evaluation of infill masonry walls influence on the dynamic behaviour of buildings: a review. *Arch Comput Methods Eng* 2022;29(6):3773–87.
- [45] Augenti N, Parisi F, Prota A, Manfredi G. In-plane lateral response of a full-scale masonry subassemblage with and without an inorganic matrix-grid strengthening system. *J Compos Construct* 2011;15(4):578–90.
- [46] Parisi F, Augenti N, Prota A. Implications of the spandrel type on the lateral behavior of unreinforced masonry walls. *Earthq Eng Struct Dyn* 2014;43(12):1867–87.
- [47] Brincker R, Ventura C. Introduction to operational modal analysis. John Wiley & Sons; 2015.
- [48] García-Macías E, Ubertini F. MOVA/MOSS: Two integrated software solutions for comprehensive structural health monitoring of structures. *Mech Syst Signal Process* 2020;143:106830.
- [49] Olsen P, Skafte A, Hansen J, Hovgaard M, Brincker R, Ventura C. Identification of systems with complex modes using OMA. In: Proceedings of the 5th IOMAC international operational modal analysis conference. 2013.
- [50] Gres S, Döhler M, Andersen P, Mevel L. Uncertainty quantification for the Modal Phase Collinearity of complex mode shapes. *Mech Syst Signal Process* 2021;152.
- [51] Lofrano E, Paolone A, Ruta G. Dynamic damage identification using complex mode shapes. *Struct Control Health Monit* 2020;27(12):e2632.
- [52] Pastor M, Binda M, Harčarik T. Modal assurance criterion. *Procedia Eng* 2012;48:543–8.
- [53] Cosenza E, Del Vecchio C, Di Ludovico M, Dolce M, Moroni C, Prota A, Renzi E. The Italian guidelines for seismic risk classification of constructions: technical principles and validation. *Bull Earthq Eng* 2018;16:5905–35.
- [54] Ministero delle Infrastrutture e dei Trasporti MIT. NTC (2018) Norme Tecniche per le Costruzioni. 2018, (in Italian).
- [55] Parisi F, Augenti N. Seismic capacity of irregular unreinforced masonry walls with openings. *Earthq Eng Struct Dynam* 2013;42(1):101–21.
- [56] Frank R. Designers' guide to EN 1997-1 Eurocode 7: Geotechnical design-general rules, vol. 17. Thomas Telford; 2004.
- [57] Hibbett K, Karlsson B, Sorensen P. Abaqus/standard: user's manual. Hibbett, Karlsson & Sorensen; 1998.
- [58] Lourenço PJB. Computational strategies for masonry structures. 1997.
- [59] D'Altri AM, Sarhosis V, Milani G, Rots J, Cattari S, Lagomarsino S, Sacco E, Tralli A, Castellazzi G, de Miranda S. Modeling strategies for the computational analysis of unreinforced masonry structures: review and classification. *Arch Comput Methods Eng* 2020;27:1153–85.
- [60] Schiavoni M, Giordano E, Roscini F, Clementi F. Numerical assessment of interacting structural units on the seismic damage: A comparative analysis with different modeling approaches. *Appl Sci* 2023;13(2):972.
- [61] Zizi M, Chisari C, De Matteis G. Effects of pre-existing damage on vertical load-bearing capacity of masonry arch bridges. *Eng Struct* 2024;300:117205.
- [62] Valente M, Milani G. Damage assessment and collapse investigation of three historical masonry palaces under seismic actions. *Eng Fail Anal* 2019;98:10–37.
- [63] Bayraktar A, Hökelekli E. Seismic performances of different spandrel wall strengthening techniques in masonry arch bridges. *Int J Architect Herit* 2021;15(11):1722–40.
- [64] D'Altri AM, de Miranda S, Castellazzi G, Glisic B. Numerical modelling-based damage diagnostics in cultural heritage structures. *J Cult Herit* 2023;61:1–12.
- [65] Valente M. Earthquake response and damage patterns assessment of two historical masonry churches with bell tower. *Eng Fail Anal* 2023;107418.
- [66] Hillerborg A, Modéer M, Petersson P-E. Analysis of crack formation and crack growth in concrete by means of fracture mechanics and finite elements. *Cement Concrete Res* 1976;6(6):773–81.
- [67] Page A. The biaxial compressive strength of brick masonry. *Proc Inst Civ Eng* 1981;71(3):893–906.
- [68] Pluijm R, van der. Shear behaviour of bed joints. In: Hamid A, Harris H, editors. 6th North American masonry conference, 6-9 June 1993, philadelphia, pennsylvania, USA. Technomic Publ. Co.; 1993, p. 125–36.
- [69] Manual AU. Abaqus theory guide. Version 6.14. USA: Dassault Systemes Simulia Corp; 2014.
- [70] Abdulla KF, Cunningham LS, Gillie M. Simulating masonry wall behaviour using a simplified micro-model approach. *Eng Struct* 2017;151:349–65.
- [71] Scacco J, Ghiassi B, Milani G, Lourenço PB. A fast modeling approach for numerical analysis of unreinforced and FRM reinforced masonry walls under out-of-plane loading. *Composites B* 2020;180:107553.
- [72] UNI. UNI EN 338. Structural Timber: Class Strength. 2016.
- [73] Ministero delle Infrastrutture e dei Trasporti MIT. Circolare 21 Gennaio 2019 n. 7 CS. LL. PP. Istruzioni per l'applicazione dell'aggiornamento delle 'Norme Tecniche per le Costruzioni' di cui al DM 17/01/2018 (in Italian). 2019, Suppl. Ord. Alla GU n. 35 Del 11/2/19.
- [74] Standard B. Eurocode 6—Design of masonry structures. London: British Standard Institution; 2005, 2005.
- [75] Asprone D, Cadoni E, Prota A, Manfredi G. Dynamic behavior of a Mediterranean natural stone under tensile loading. *Int J Rock Mech Min Sci* 2009;46(3):514–20.
- [76] Parisi F, Lignola G, Augenti N, Prota A, Manfredi G. Nonlinear behavior of a masonry subassemblage before and after strengthening with inorganic matrix-grid composites. *J Compos Construct* 2011;15(5):821–32.
- [77] Augenti N, Parisi F. Constitutive models for tuff masonry under uniaxial compression. *J Mater Civ Eng* 2010;22(11):1102–11.
- [78] Marcari G, Basili M, Vestroni F. Experimental investigation of tuff masonry panels reinforced with surface bonded basalt textile-reinforced mortar. *Composites B* 2017;108:131–42.
- [79] Guadagnuolo M, Aurilio M, Basile A, Faella G. Modulus of elasticity and compressive strength of tuff masonry: Results of a wide set of flat-jack tests. *Buildings* 2020;10(5):84.